



HAL
open science

Experimental characterization of tensile and compressive translaminar fracture toughness coupling multi-physics measurements

R Rutar, J Serra, Q Bausiere, C Bouvet

► To cite this version:

R Rutar, J Serra, Q Bausiere, C Bouvet. Experimental characterization of tensile and compressive translaminar fracture toughness coupling multi-physics measurements. *Engineering Fracture Mechanics*, In press, 10.1016/j.engfracmech.2023.109568 . hal-04190997

HAL Id: hal-04190997

<https://hal.science/hal-04190997>

Submitted on 30 Aug 2023

HAL is a multi-disciplinary open access archive for the deposit and dissemination of scientific research documents, whether they are published or not. The documents may come from teaching and research institutions in France or abroad, or from public or private research centers.

L'archive ouverte pluridisciplinaire **HAL**, est destinée au dépôt et à la diffusion de documents scientifiques de niveau recherche, publiés ou non, émanant des établissements d'enseignement et de recherche français ou étrangers, des laboratoires publics ou privés.

Experimental characterization of tensile and compressive translaminar fracture toughness coupling multi-physics measurements

R. Rutar¹, J. Serra¹, Q. Bausiere^{1,2}, C. Bouvet¹

1 : Université de Toulouse, Institut Clément Ader (UMR CNRS 5312), ISAE-SUPAERO / INSA /
IMT Mines Albi / UPS
10 av. E. Belin 31055 Toulouse Cedex 4, France
2 : Airbus Operations
316 Route de Bayonne, 31300 Toulouse, France

Address for correspondence: christophe.bouvet@isae-superaero.fr

Abstract

The study of the failure modes of carbon fiber reinforced polymers is essential due to their extensive use in industry. Translaminar failure (at the scale of the laminate) has been studied extensively the main goal being to compute the critical strain energy release rate in mode I of the ply G_{IC_ply} but large variations can be observed between papers. This study investigates this failure mode of a carbon/epoxy laminate, using Compact Tension (CT) and Compact Compression (CC) specimens. The stacking sequence used is $[45/-45/(0/90)_4]_s$ where 45° plies on the outside efficiently prevented the buckling of the specimen to be observed, as well as plasticity of the matrix. Moreover, this layup is rather similar to real-life industrial stacking sequences. Strains fields and axes displacement were obtained using digital image correlation. Infrared images were used to follow the crack propagation during the loading of the specimen and compared to DIC and X-ray tomography crack length measurements. IR measurements studied from a qualitative point of view were thus shown to be an efficient and reliable method. G_{IC} of the laminate G_{IC_lam} was computed with both the ASTM-E399 and compliance methods, and finally G_{IC_ply} was computed using a rule of mixtures. Secondary damage was detected and its effects on the energy dissipated were quantified using strain fields, X-ray and infrared images. This enabled a more accurate rule of mixtures to be redefined. The failure scenarios of all specimens were eventually exhibited. G_{IC_ply} values in tension were found to be higher than in the literature whereas in compression it was found to be lower than in the literature, due to crack propagation being detected earlier by means of IR measurements.

1. Introduction

The reduction of aircraft weight is a major concern for aircraft manufacturers, as it is a way of reducing the fuel burn and thus the carbon footprint of the aviation sector. Composite materials allow for a substantial weight reduction thanks to their high strength-to-weight ratio. Today, Carbon Fiber-Reinforced Plastics (CFRP) are among the most efficient known materials. This has created a need for a deeper understanding of the failure mechanics of these materials. At the mesoscopic scale, CFRP failure results from 3 primary types of damage: interlaminar, intralaminar, translaminar

[1]. Intralaminar failure occurs when damage propagates parallel to the fibers, inside the ply. Interlaminar failure happens when a crack propagates between two plies (delamination). Translaminar failure occurs when the crack propagates through the thickness of the laminate. This is the most energetic failure mode.

5 Compact Tension (CT) and Compact Compression (CC) tests were first developed for metallic materials (ASTM-E399 test method), but many studies have been carried out to adapt them to test composites [1,2,3]. CT and CC tests have been widely used to study the translaminar fracture in mode I of composites, as they allow a stable crack propagation. CT tests are difficult to analyze and understand, because of secondary damage (i.e. damage not directly linked to the crack growth) [3]
10 and because of the complexity of the failure scenario. Another definition of secondary damage could be any damage not linked to translaminar crack propagation and induced by the experimental setup (Figure 9).

Failure of CC specimens is even more complicated to understand, and if the CC test allows the measurement of the critical strain energy release rate (SERR) at initiation, several articles show that
15 extracting the value in propagation is complicated due to crushing in the specimen in the areas where the crack has already propagated [2,4]. Fewer studies have been conducted on CC than on CT.

Several methods have been used regarding the experimental testing procedures.

The crack length monitoring value is essential in order to calculate the exact G_{IC} value, as a small uncertainty in this value can lead to a significant error in the final calculation [5]. Many methods are available to measure it. The first one, used by [1,3,5] is the simplest. It consists in filming a face of the specimen painted white, to visually estimate the crack length. However, Laffan et al. [5] noted that this method could suffer from a lack of precision. DIC can also be used. This is the method chosen by [2,6], where software detects the discontinuities in the strain field, then the path of the
25 crack can be visualized and analyzed. Reiner et al. [7] also used DIC but with a maximum strain criterion. It is assumed that the material has failed when the strain measured on the surface of the specimen exceeds the strain threshold given by the manufacturer, in tension or in compression. However, these DIC methods need to assume that strains and discontinuities measured on the surface of the specimen are representative of the state of the specimen through the thickness,
30 which may not be the case with a specimen exhibiting delamination. Gonzalez et al. [8] compared the Tsai-Hill criterion computed using DIC measurements and X-ray tomography images to estimate the crack length in each ply orientation. This technique enables the crack length in individual plies to be measured and showed a large dispersion in different plies. In situ X-ray measurements were recently successfully used by (Sun, 2020) to measure, at any loading point, the crack length to build
35 a partial R-curve on a single edged notched tension specimen.

Laffan et al. [5] used the modified compliance method to calculate this value. Several specimens with a known crack length are manufactured, and their compliance is measured. This compliance is then approximated with this function:

$$C = (\alpha * a + \beta)^x$$

with α , β , χ parameters which must be estimated, and a the crack length. Eventually, the effective crack length can be calculated by measuring the compliance of the specimen during the test:

$$a_{eff} = \frac{C^{\frac{1}{\chi}} - \beta}{\alpha}$$

This method has the drawback of assuming that a specimen whose crack was cut is representative of a specimen whose crack is obtained by loading. This may not be the case due to damage around the crack as they may influence the compliance of the specimen.

Another method to measure the crack length is by using an infrared camera. When a failure occurs (and particularly fiber failure), heat is released, and it can be identified on the thermal signature of the specimen. The localization of the damage zone can be determined, then the crack length is calculated. This is the method described by Saadati et al. [9]. However, comparing the crack length obtained using IR measurement to other measurement methods has rarely been carried out, as IR thermography methods are usually preferred when it comes to computing the critical SERR [9,10]. Another advantage of IR images is that they can detect damage that happened over a short period of time (such as fiber failure) thanks to the thermal signature, thus this technique can be interesting from a qualitative point of view. More precise infrared values can also be taken to calculate the G_{IC} locally [10].

Other measurements can be taken during tests on carbon/epoxy materials, such as acoustic emission [1,11] to identify the type of damage the specimen is undergoing.

Data reduction methods for CT and CC tests are numerous and complex. They mostly aim at calculating the critical SERR G_{IC} . The ASTM-E399 method was originally developed for isotropic linear-elastic metallic materials, and its application to composite materials is not trivial. It has been used in numerous studies [2,3,12,13]. Laffan et al. [5] underlined that this method could not be directly used for orthotropic materials. Moreover, Pujols Gonzalez et al. [2] observed that this method underestimates the value of G_{IC} if the material presents a large plasticity area before the first failure for CT tests but found consistent values for CC tests. (Rondina, 2023) came to the opposite conclusion; the ASTM-E399 method gives consistent results for CT tests, contrary to CC tests.

The area method is simple to use. However, as noted by Laffan et al. [5,12,13], this method is sensitive to Δa measurement errors, especially for low Δa values. The calibrated compliance method uses the Irwin-Kies formula, with an approximation of the compliance vs a function. This method is often considered as more reliable than the previous ones [1,2,5,14], (Rondina, 2023) for CT tests. A method based on the calculation of the J-integral is also possible [6], (He, 2022). According to [5], this method has the advantage of not having to derive the interpolated function $C(a)$, possibly reducing the errors for CT tests. However, [6] observed that this method was not applicable for CC tests because of the high plasticity induced by the formation of kink bands. More recently, (Xu, 2021) used a finite element model on Over-height Compact Tension specimens to compute the R-curve using VCCT, informed by the loadings measured at failure. However, this

technique has the drawback of having to model the shape of the crack, which can lead to uncertainties.

5 Some studies focused on methods to prevent secondary damage, mainly by changing the geometry of the CT specimen [15] or CC specimen [17]. However, only qualitative studies were carried out, the energy that could be dissipated through these secondary damages was not estimated. Most of the studies [1,4,5] use the rule of mixtures to compute the critical SERR of the ply from the value of the laminate; however, such a simple model can be questioned in the face of the complex failure scenario exhibited by both CT and CC tests.

10 All these studies showed a large dispersion in G_{IC} values, according to the test methods, material used, or geometry used. No clear consensus has been reached on how to carry out CT and CC tests. The different methods of crack length measurement, especially the use of IR images from a qualitative point of view, need to be explored and compared to each other. As phenomena leading to crack propagation are complex, estimating the energy dissipated through ways other than fiber failure is at stake to have a consistent value of the critical SERR. X-ray images allow precise and reliable measurement of the crack length and can be considered as a reference for other techniques. The phenomena leading to failure being very complex, computing the SERR of the ply from the SERR of the laminate is not simple and requires in-depth understanding of the failure phenomena.

15 Extensive testing using different techniques is thus needed to better understand the underlying phenomena.

20 A new stacking sequence for CT/CC tests is proposed below in order to mitigate buckling and matrix plasticity while being closer to real-life industrial stacking sequences. An innovative approach combining qualitatively used infrared imaging, X-ray microtomography and digital image correlation is developed to tackle the lack of understanding of the failure phenomena. A new method to estimate the energy actually released by crack propagation is made possible thanks to an in-depth understanding of the failure scenario.

Objectives of the study:

30 The goal of this study is to analyze the translaminal fracture toughness of a carbon fiber reinforced thermoset material (carbon/epoxy). CT and CC specimens will be used to study respectively tensile and compressive damage. Three methods of crack length measurement will be analyzed and compared: infrared, DIC and X-ray tomography. The failure scenario will eventually be detailed. Particular attention will be paid to detecting secondary damage using IR and DIC measurements as well as X-ray microtomography images, and the energy dissipated through these damages will be estimated. The critical SERR in mode I G_{IC} (opening mode) of the laminate $G_{IC,lam}$ will be calculated with different methods. Then, the critical SERR of the ply $G_{IC,ply}$ can be computed using the rule of mixtures and by taking into account actual damage and energy dissipated through secondary damages observed using X-ray microtomography.

2. Experimental tests

2.1. Manufacturing the specimens

5 The material used is carbon/epoxy UD prepreg with mechanical properties close to T700/M21. The exact reference of the material cannot be given for reasons of confidentiality. The stacking sequence is $[45/-45/(0/90)_4]_s$, for a total of 20 plies (in this article, the 0° axis is defined as the loading axis). A CT/CC specimen must have as many 0° plies as possible, as the goal is to measure the translaminar fracture toughness of the fibers. The $\pm 45^\circ$ plies in the surface delay buckling, and can take up shear efforts, thus avoiding the formation of a large plasticity area (which can be observed on orthotropic laminates [2]). This type of stacking sequence has rarely been studied, as 0° and 90° plies are often placed on the surface of the specimen to facilitate crack length measurement. The use of IR measurements enables us to use this stacking sequence.

15 The laminate sheets were manufactured using pre-preg hand lay-up. The geometry of CT and CC specimens respectively can be seen on Figure 1. They were, including the holes, cut out of a laminate sheet using a water jet cutting machine. The holes were then drilled to the correct diameter with carbide drill bits. Then a 1 mm long and 0.3 mm wide initial notch was made using a diamond-coated wire saw. The diameter of the tip of this notch was 0.3 mm, which is smaller than 0.5 mm to avoid any dependency of the initiation fracture toughness on the notch tip radius [12,13].

20 The tests were carried out on two specimen geometries (Figure 1). The first had 11.25 mm diameter holes (geometry usually used for CT/CC tests and given by the ASTM_E399 standard [2]). The choice of this standard instead of the ASTM_E1922 is due to the possibility for the crack to propagate for a longer distance with the compact tension/compression geometry [26], thus enabling a greater part of the R-curve to be computed, as noted by [1]. For this one, aluminium spacers were used so that they could be loaded with 8 mm axes. However, this design resulted in early failure around the loading holes, which makes this test unsuitable (Figure 11). Therefore, a second geometry with 8 mm diameter loading holes was used.

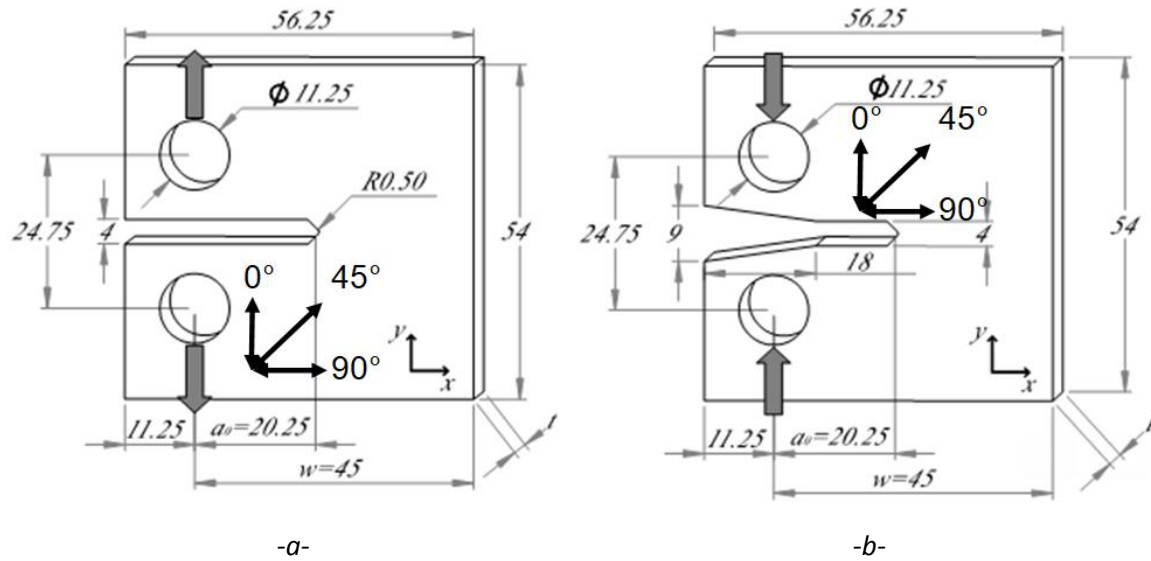


Figure 1 : Dimensions of a CT specimen with 11.25 mm loading holes (a) and of a CC specimen with 11.25 mm holes (b)

5

The geometry used results in an a_0/w ratio equal to 0.45, where a_0 is the initial notch length and w the distance from the loading hole centers to the right edge of the specimen.

A DIC pattern is painted on one side of the specimen, with an acrylic based spray paint. The pattern is non-periodic (i.e. as random as possible), and care was taken during painting to ensure that no preferred direction was created (i.e. the pattern has to be as isotropic as possible). In practical terms the pattern has to be as random as possible to make every area of the structure as unique as possible. Otherwise, the correlation that consists in identifying the area around a point of interest (often called subset) in every snapshot taken during the test, can be difficult because several solutions are found instead of one single one. The size of the speckle was as close as possible to 3-4 pixels, as advised by Reu P. [17]. The paint was applied just before the test, to prevent chipping of the paint.

On the other side, a matt black paint was applied to ensure a maximum and homogeneous emissivity, to have consistent results with the infrared camera.

2.2. Test configuration

The tests were carried out on an Instron 5989 screw-driven traction testing machine, with a setup capable of applying a load up to 100 kN in traction and in compression. The forces are measured by a 50 kN loading cell. For confidentiality reasons, the measured forces are normalized using the maximum measured load and the precise name of the material cannot be given, it can only be said that it is a carbon/epoxy UD laminate. The experimental setup can be seen on Figure 2.

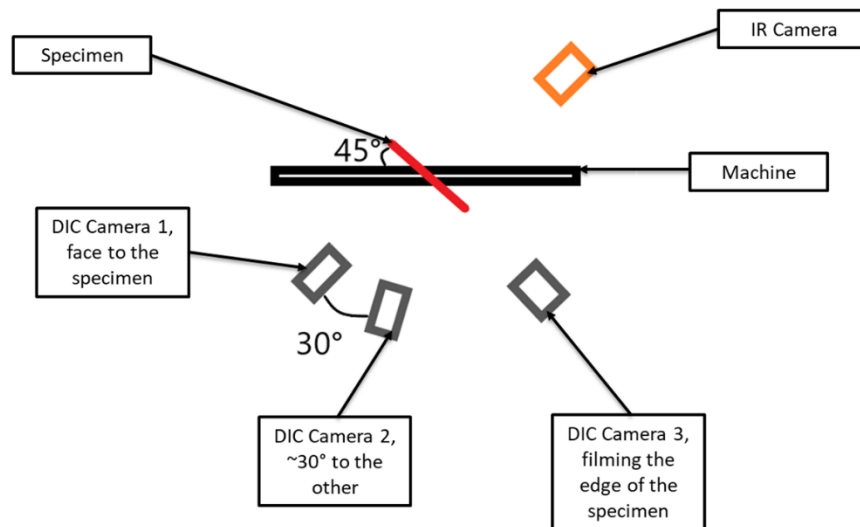


Figure 2 : Experimental setup of the second test campaign

Two test campaigns were carried out. The first one was composed of CC and CT tests, with 11.25 mm holes and 8 mm holes, with two specimens of each type. Specimens from this campaign with 8 mm holes will be subsequently referred to as CT1&2 and CC1&2. The second test campaign was only composed of CT and CC specimens with 8 mm holes, with 4 specimens of each type. They will subsequently be referred to as CT3 to 6 and CC3 to 6. The second experimental setup was slightly different to study the phenomena observed during the first test campaign in more detail.

For both campaigns, a Telops FAST thermal camera with a resolution of 256x320 pixels was placed on the other side of the specimen, and a black sheet was placed in the field of the camera behind the specimen to make sure the measurements could not be disturbed by any heat source. The acquisition time was around 80 μ s for all tests.

The first test campaign experimental setup had two 5 Mpx Pike f-505B monochrome cameras. The mounted lenses have a 50 mm focal length. The first was placed perpendicular to the specimen, to make sure the 2D displacements are measured with as little error as possible. The second was placed on the same rack but with a 30° angle to measure possible out-of-plane displacements using stereo-correlation, in order to make sure no buckling of the specimen occurred. A light source was placed above each camera.

For the second test campaign, a third 5 Mpx Pike f-505B monochrome camera was added perpendicular to the specimen to film the side opposite the loading axis. The goal was to measure the compressive and tensile strains to detect secondary damage (see 5.iii). The two other cameras were replaced by 8.9 MPx cameras.

For the first test (CT1- 11mm, see Table 1), the frequency of the cameras was set to 2Hz, and that of the thermal camera was set to 100 Hz. The loading speed was set to 1 mm/min. For all the other tests, to reduce data volumes, the frequency of the cameras was set to 2Hz, and that of the thermal camera to 10 Hz. The loading speed was set to 2 mm/min.

The steel loading pins were also painted on the sides with the same pattern as the specimens, to measure the axis displacement accurately. For the first test campaign, the paint was applied on the specimens the day before the test. However this resulted in extended paint chipping. Applying the paint less than 20 minutes before the test solved this issue for the second test campaign. Two aluminum spacers were used to center the specimen in the loading devices.

The test configuration corresponding to each test is summed up in Table 1.

Test	DIC camera 1	DIC camera 2	DIC camera 3	IR camera	Holes diameter	Loading speed
CT1-11 mm	5 MPx, 2 Hz	5 MPx, 2 Hz	None	100 Hz	11 mm	1 mm/min
CT2-11 mm	5 MPx, 2 Hz	5 MPx, 2 Hz	None	10 Hz	11 mm	2 mm/min
CT1	5 MPx, 2 Hz	5 MPx, 2 Hz	None	10 Hz	8 mm	2 mm/min
CT2	5 MPx, 2 Hz	5 MPx, 2 Hz	None	10 Hz	8 mm	2 mm/min
CT3	8.9 MPx, 2 Hz	8.9 MPx, 2 Hz	5 MPx, 2 Hz	10 Hz	8 mm	2 mm/min
CT4	8.9 MPx, 2 Hz	8.9 MPx, 2 Hz	5 MPx, 2 Hz	10 Hz	8 mm	2 mm/min
CT5	8.9 MPx, 2 Hz	8.9 MPx, 2 Hz	5 MPx, 2 Hz	10 Hz	8 mm	2 mm/min
CT6	8.9 MPx, 2 Hz	8.9 MPx, 2 Hz	5 MPx, 2 Hz	10 Hz	8 mm	2 mm/min
CC1	5 MPx, 2 Hz	5 MPx, 2 Hz	None	10 Hz	8 mm	2 mm/min
CC2	5 MPx, 2 Hz	5 MPx, 2 Hz	None	10 Hz	8 mm	2 mm/min
CC3	8.9 MPx, 2 Hz	8.9 MPx, 2 Hz	5 MPx, 2 Hz	10 Hz	8 mm	2 mm/min
CC4	8.9 MPx, 2 Hz	8.9 MPx, 2 Hz	5 MPx, 2 Hz	10 Hz	8 mm	2 mm/min
CC5	8.9 MPx, 2 Hz	8.9 MPx, 2 Hz	5 MPx, 2 Hz	10 Hz	8 mm	2 mm/min
CC6	8.9 MPx, 2 Hz	8.9 MPx, 2 Hz	5 MPx, 2 Hz	10 Hz	8 mm	2 mm/min

Table 1 : Experimental setup corresponding to each test

3. Experimental data analysis methods

3.1. Measuring the axis displacement

Measuring the displacement of the loading axes is essential when using methods such as the area method or the compliance method [5]. The easiest way to access this value is via the value given by the machine. However, it can be imprecise, or may need to be corrected using the machine compliance [1]. Another way to get this value is by using an extensometer [18,19]. Another method is image correlation. This is the method chosen by [2,3]. The specimen is filmed by a camera. Software then processes the sequence of images, identifying numerous small regions (subsets), and computing their displacements. This is the method used in this article, the circles on which the axis displacements were averaged can be seen in Figure 5.

3.2. Measuring the crack length

The first method chosen to measure the crack length was the use of infrared images. They offered good precision, particularly for CC tests, as can be seen on Figure 3. When the spot is small, the crack tip is assumed to be located at the center of the spot. In this case, the width of the spot is due to heat diffusion and not to diffused damage (Figure 3). It is considered that local heating in the

order of magnitude of 1°C shows fiber failure (which is the order of magnitude of the heating observed by [10] for this failure).

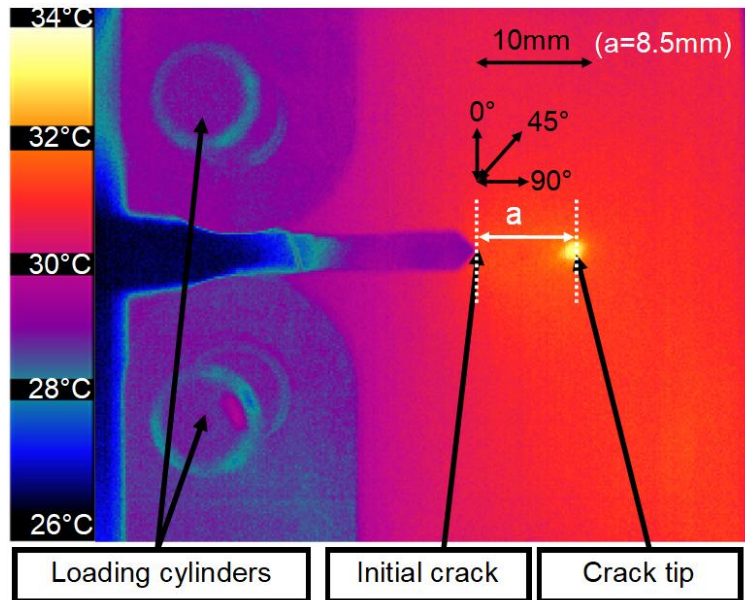


Figure 3 : Local heating of CC2 specimen on the tip of the crack after failure. (Surface ply at 45°)

5

The damage is more diffused for the CT specimen. Another method was therefore used to calculate this length. The method consists in taking the distance according to the horizontal direction between the notch beginning and the center of the heat dots. However, since multiple spots appear at the same time for the CT, it was decided to measure the distance with the furthest dot from the notch start, as can be seen in Figure 4. As for the CC tests and for the same reasons, the center of the heated dot is assumed to be the tip of the crack. Furthermore, the failure is mainly driven by 0° plies, but since the heat mainly diffuses along the fiber direction, the temperature rise detected by the thermal camera appears blurry in the beginning. It was therefore chosen to measure the length only when clear dots appear after the first temperature rise (in general 100-200 ms later). No other fiber damage appears during this interval, since the delay between two load drops on the curves (for the CT specimens) is at least a few seconds.

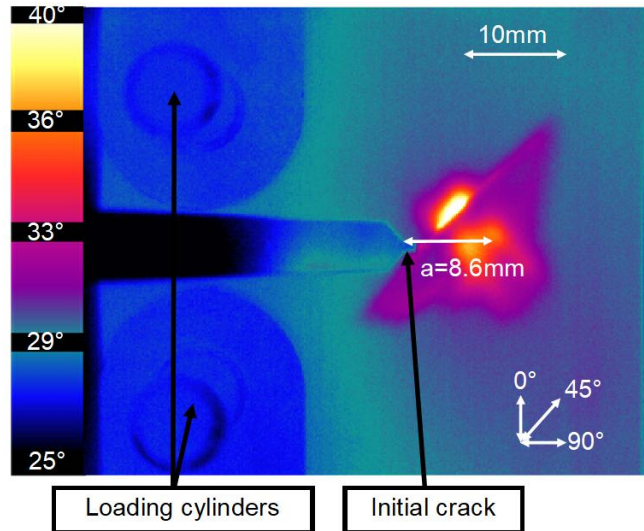


Figure 4 : Local heating of the surface of a CT specimen after failure. The white arrow indicates the distance used to measure the crack length. (Surface ply at 45°)

5 The second method uses DIC measurements. Strain fields are calculated using digital image correlation (DIC) with the VIC-2D[©] software. The size of the subset was chosen to minimize the error σ , while keeping a subset size small enough to have information on the frontiers of the specimen.

10 Considering the experimental setup of the first test campaign and the pattern precision, a subset size of 21 pixels, a step size of 5 pixels and a Lagrange filter size of 5 subsets were used. This results in a maximum σ error approximately equal to 0.04 pixels. With a pixel size equal to $p=0.028\text{ mm}$, this corresponds to a displacement error approximately equal to $\sigma * p = 1.1\ \mu\text{m}$, which is acceptable.

These choices lead to a square virtual gauge with a side size of 1.3 mm, according to the formula given by the VIC-2D[©] user manual. The virtual gauge size can be seen in Figure 5.

15 It is assumed that the material has failed when the strain measured along the y axis on the surface of the specimen exceeds the strain threshold given by the manufacturer, in tension or in compression (supposedly showing fiber failure in the 0° plies). For reasons of confidentiality, strains were normalized with the manufacturer's maximum allowable strain, in tension for positive strains, in compression for negative strains. An example for CT and CC specimens can be seen in Figure 5.

20 Purple shows areas where the strain in compression is lower than the minimum allowable value in compression, red in Figure 5 (a) shows areas where the strain in tension is over the allowable value.

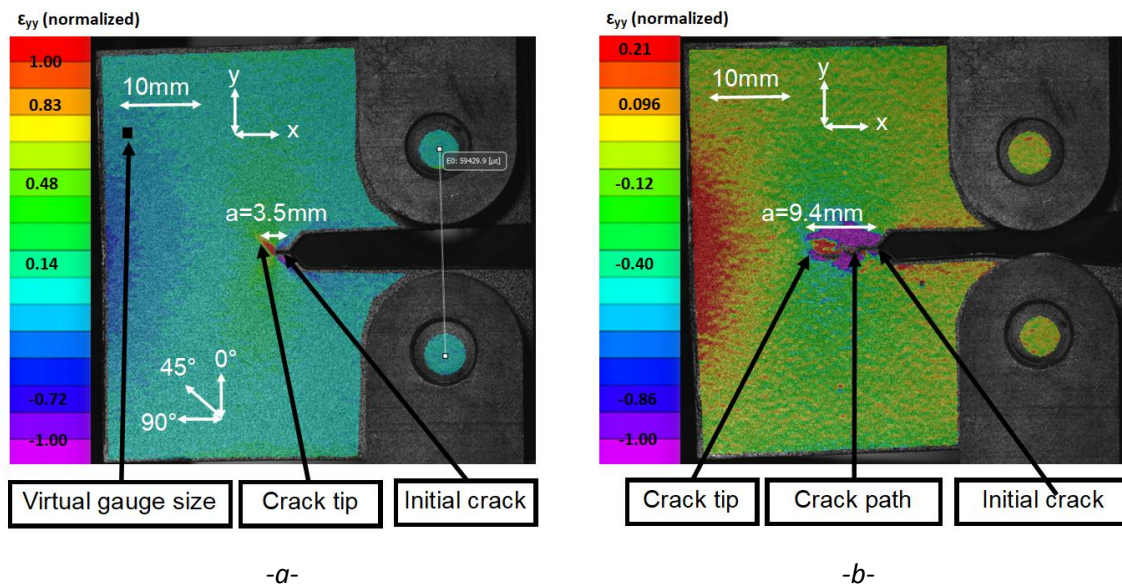


Figure 5 Crack length measurement using strain criterion on CT2 specimen (a) and on CC2 specimen (b) (surface ply at 45°). The white arrow indicates the crack length. The black square shows the size of a virtual gauge

5

The last method is X-ray microtomography. As this measurement is carried out after the test, only one single value is available per specimen. This method was used on CT4, CC5&6. The size of the voxel was set to $10\ \mu\text{m}$. Two methods can be considered and will be compared to define the tip of the crack. It can be defined at the point where every 0° ply exhibits fiber failure (Figure 6) or at the point where at least one 0° ply exhibits fiber failure (Figure 7).

10

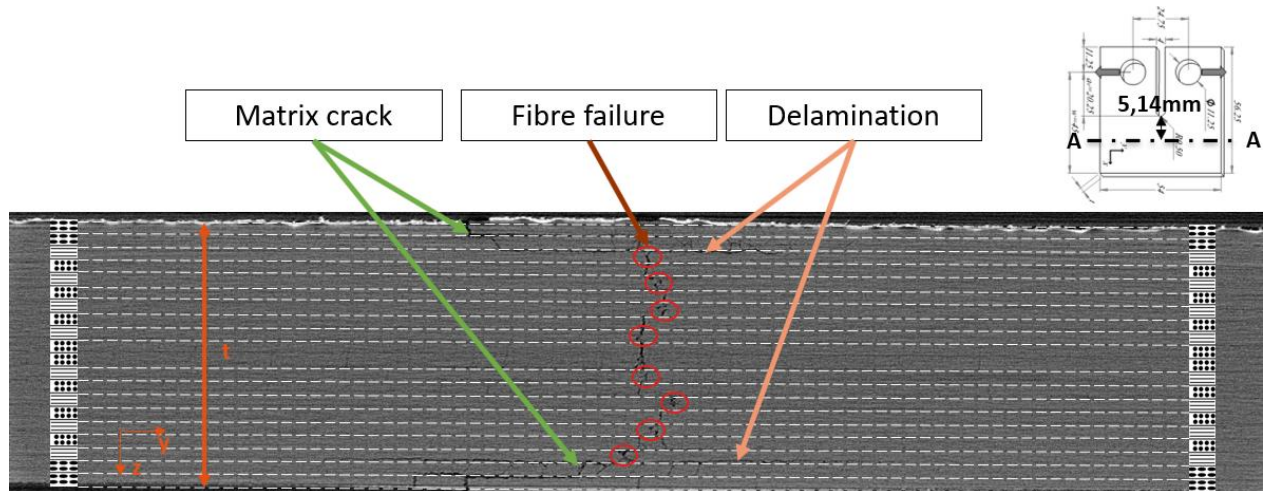


Figure 6 : X-ray tomography A-A cut of CT4, where every 0° ply exhibits fiber failure (circled in red)

$$C_I = \sqrt{\frac{1}{E_x E_y}} \sqrt{\sqrt{\frac{E_y}{E_x} - \nu_{yx}} + \frac{E_y}{2G_{xy}}}$$

with E_x the longitudinal Young's modulus of the laminate (perpendicular to the loading axis), E_y the transverse Young's modulus (parallel to the loading axis), ν_{xy} Poisson's ratio, and G_{xy} the shear modulus. These values are computed using the laminate theory and the ply properties E_l , E_t , ν and G_{lt} .

- 5 This method only gives the G_{IC_lam} value for the initiation. Indeed, this method is based on a certain crack shape being assumed, which is not respected once the crack has started propagating due to extensive and complex damage.

3.3.2. The compliance method

This method is used to calculate the critical SERR using the Irwin-Kies formula [21]:

$$G_{IC} = \frac{F^2}{2b} * \frac{\partial C}{\partial a}$$

- 10 with F the force applied to the specimen just before the failure, C the compliance of the specimen and a the crack length.

To apply this method, the force, displacement, and crack length values are taken just after each crack propagation. Then, the compliance C as a function of the crack length a is approximated with the following function:

$$C(a) = \beta + \alpha a^3$$

- 15 (Equation 1)

α and β are estimated by plotting C as a function of a^3 , then a linear regression is performed to estimate α and β .

Then, G_{IC_lam} can be calculated as:

$$G_{IC_lam} = \frac{3F^2}{2b} * a^2$$

- 20 In this method, the approximation of C as a function of a is essential. Other models can be implemented to get consistent values. The cubic model described above will be compared to other models, to have the best possible approximation.

First, a power law used by [1,5]:

$$C(a) = (\beta + \alpha a)^x$$

(Equation 2)

Davila et al. [14] describe the process to estimate these values. The χ parameter is estimated by plotting $C(a)^{(1/\chi)} = (u_a/F_a)^{(1/\chi)}$ versus a , where F_a and u_a are respectively the force and displacement corresponding to a crack of length a . The parameter χ is then adjusted so that the curve $C(a)^{(1/\chi)}$ vs a is as close as possible to an affine function. Eventually, α and β are estimated by calculating a linear regression on $C(a)^{(1/\chi)}$, where α is the slope of the affine function and β its ordinate at the origin.

The last law which will be used is derived from a polynomial law:

$$C(a) = \beta + \alpha a^\chi$$

(Equation 3)

Where α , β , χ are directly estimated to best fit the data. In this equation, χ isn't necessarily a whole number. For each test, a comparison will be done to select the law best fitting each data set. For the last two methods, when parameters must be estimated, the Matlab[®] Curve Fitting Toolbox will be used. A custom equation corresponding to the law is parameterized. Eventually, the Levenberg-Marquardt algorithm is used to fit the data with the desired equation [22].

3.3.3. Rule of mixtures

Teixeira et al. [1] describe the calculation of the G_{IC_ply} values using the rule of mixtures. The G_{IC_lam} value can be calculated using the individual $G_{IC}^{(i)}$ of each ply.

$$G_{IC_lam} = \sum_{i=1}^N G_{IC}^{(i)} * \frac{t_i}{t}$$

Where N is the total number of plies, t_i is the thickness of the ply i , and t is the total thickness of the laminate. The G_{IC} of the 90° plies will be considered as negligible since the fracture of these plies is mainly driven by the matrix (G_{IC} of the matrix around 100 times smaller than that of the fibers). The G_{IC} of the 0° plies is equal to the critical SERR of the ply G_{IC_ply} . Eventually, the G_{IC} of the +/-45° plies is equal to $G_{IC_ply}/\sqrt{2}$, since for a given crack length a , the effective length of broken fibers is equal to $a/\sqrt{2}$ if a step-like propagation scheme in these plies is assumed (Figure 8).

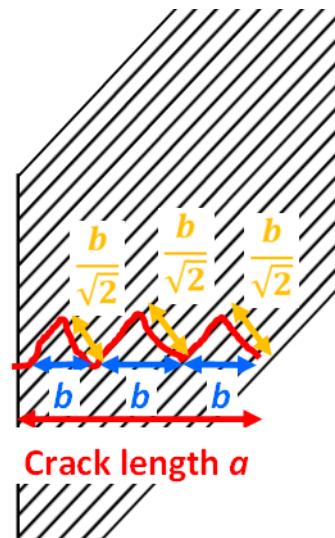


Figure 8 : Computation of the broken fibers length for a given crack length in the +/-45° plies

For the stacking sequence considered $([45/-45/(0/90)_4]_s)$, the final expression is as follows :

$$G_{IC_lam} = (8 G_{IC_ply} + \frac{4}{\sqrt{2}} G_{IC_ply}) / 20 \Rightarrow G_{IC_ply} = 1.85 * G_{IC_lam}$$

(Equation 4)

5 3.4. Secondary damage

Secondary damage (i.e., damage to the specimen which is not directly linked to the crack growth) can appear on the specimen and interfere with the strain energy restitution rate calculation, by dissipating energy, thus artificially modifying the value of G_{IC_lam} . Blanco et al. [15] studied this phenomenon on CT specimens, and identified several potential damage areas visible on Figure 9.

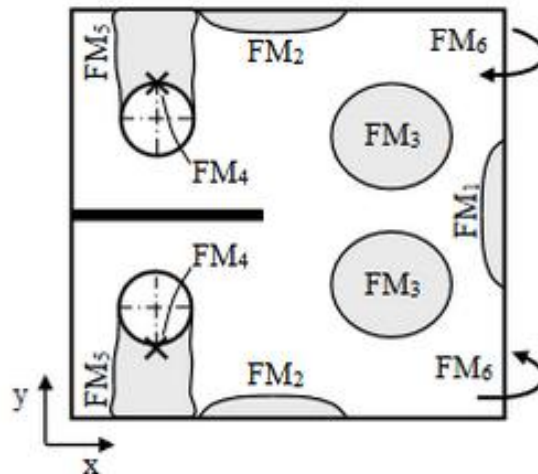
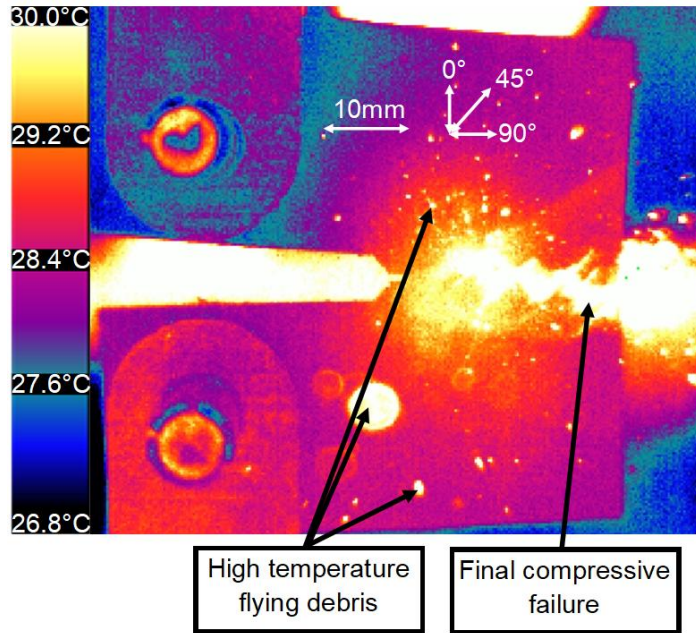


Figure 9 : Secondary damage on a CT specimen (from [15])

Each FM circled zone is linked to a potential secondary damage that can appear in this area. Fiber failure due to longitudinal compressive stress in FM1 and FM2, matrix cracking because of in-plane

shear stress in FM3, bearing in the holes at both FM4 points, shear-out in FM5, and eventually out-of-plane displacement due to buckling in FM6. Compressive damage on the opposite side of the specimen (FM1) is usually the first secondary damage that could be detected in our specimens (Figure 10). This failure is highly energetic, thus numerous flying debris were generated. High temperature shapes can be observed on Figure 10, which are the image of these debris flying out of the focal plane of the thermal camera, hence the circle shape. The test was ended when heating in a secondary damage area could be detected on IR images.



10 *Figure 10 : Secondary damage (compression on the opposite side) on CT3 specimen with 8mm holes (Surface ply at 45°)*

15 Secondary damage could be observed around the holes for the CT specimen with 11.25 mm holes (Figure 11). Contrary to what Blanco et al. [15] identified, the damage is located on the inside of the holes. This type of damage has been observed on both tested CT specimens with 11.25 mm. This damage is caused by the small distance between the bottom of the hole to the edge of the specimen. As a result, 8 mm holes were used.

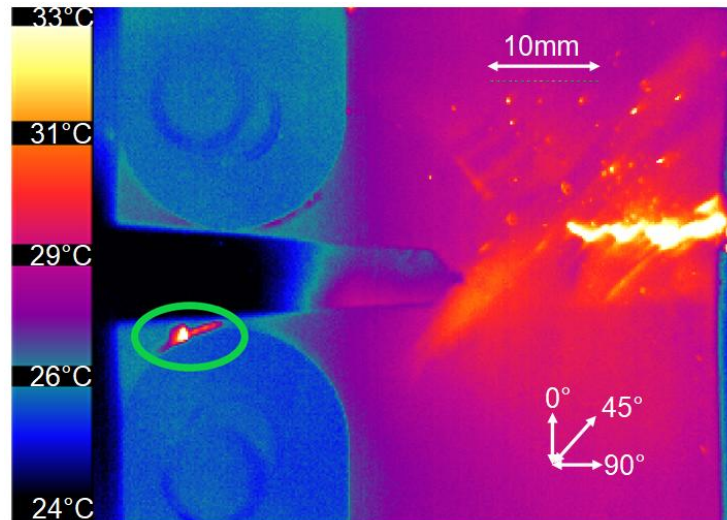


Figure 11 : Secondary damage (failure on the side of the holes, circled in green) on the first tested CT specimen with 11.25mm holes (Surface ply at 45°)

- 5 Moreover, as most of the surface around the holes is hidden behind the loading devices, it is impossible to be sure no other damage occurred during crack propagation. Consequently, CT specimens with 11.25 mm holes were not further studied. Secondary damage is less likely to be observed on CC tests. Bearing in the loading holes and tensile damage on the opposite side of the specimen are the two main types of damage that could appear on a CC specimen [16].
- 10 To detect this damage for CT and CC, strain fields were used, in combination with the infrared images. Out-of-plane displacements obtained using stereo-correlation were used to detect buckling of the specimen (FM6).

4. Compact Tension (CT) tests results

15 4.1. Force/displacement curves

The first measurements that can be obtained are the force/displacement curves, with the methods detailed before. The results are visible in Figure 12. For confidentiality reasons, results were normalized using the maximum measured load for all tests.

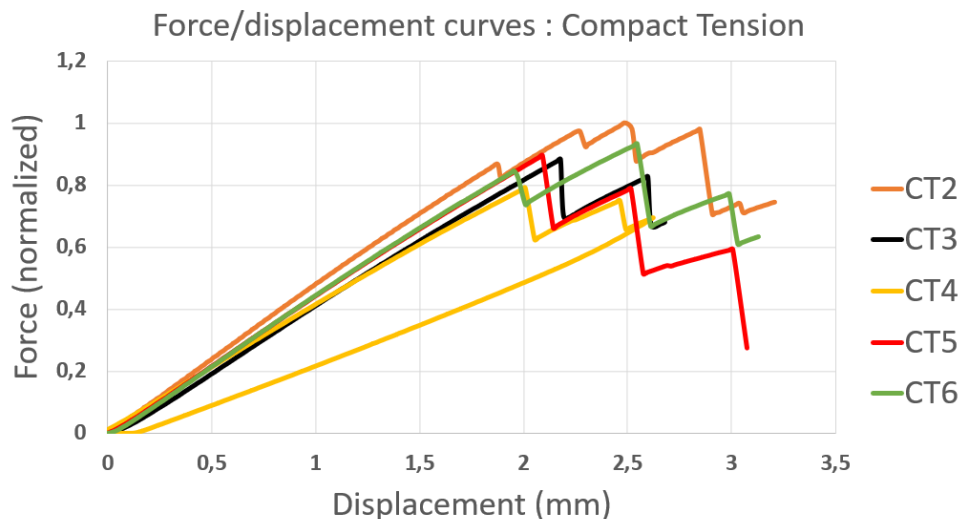


Figure 12 : Force/displacement curve for CT tests (Normalized)

The first CT test (CT1) was excluded from the results because of a wrong setting on the machine leading to inconsistent results. CT4 was stopped at a 2.6 mm-displacement to get an X-ray view of the specimen during crack propagation. The unloading path was recorded. CT2, 3, 5 and 6 were terminated when a damage other than tensile failure on the supposed crack path was observed on IR measurements (Figure 10).

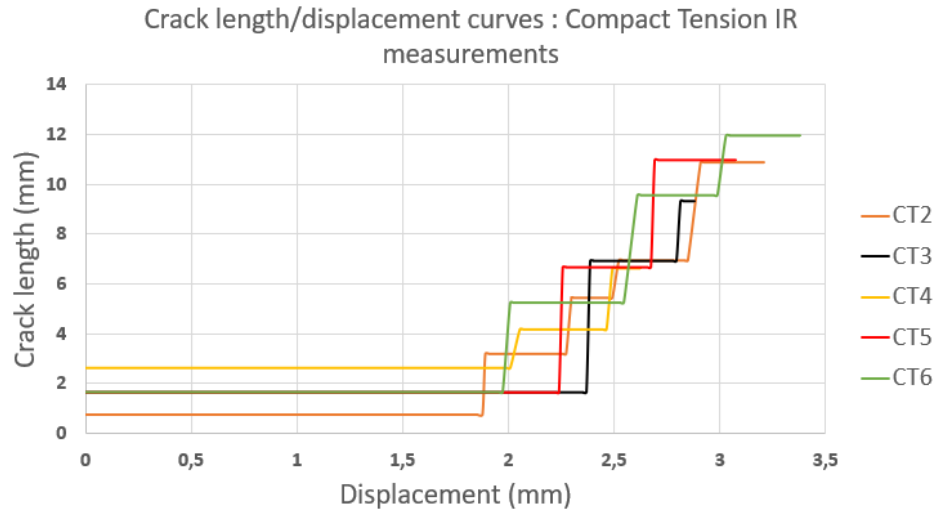
The first load drop, corresponding to the first fiber failure and thus the first measured crack growth, happens at an average force of 0.85, with a RSD (relative standard deviation) of 5.1%. From this point, a large dispersion of the curves can be observed. It can be explained by the complex failure scenario due to the presence of 45° plies, as noted by [1] who showed that when a specimen is partially made from 45° plies, failure mechanisms are more complex.

The final compressive failure occurred for CT2, 5 and 6 for an average displacement of 3.22 mm, with a very low dispersion (RSD equal to 5.0%). However, it can be noted that CT3 failed in compression for a much lower displacement than other tests. This is due to a small defect caused by the entry of the water stream during the cutting process, causing a stress concentration in the compression loaded area.

4.2. Crack length/displacement curves

The crack length vs displacement curves estimated using IR images with the method detailed previously can be seen in Figure 13. The curves do not start from a null crack length because of the machined pre-crack length. The first large propagation occurs for displacements between 1.87 and 2.37 mm, resulting in an average of 2.1 mm with a RSD equal to 9.5%. It should be noted that the first crack propagation visible in Figure 13 corresponds to the first load drop visible in Figure 12. More generally, for the CT tests, each crack length increase corresponds to a large load drop. The first crack propagation is large and dispersed compared to the size of the specimen, with an average of 3.56 mm and a RSD of 45%.

Another phenomenon that can be observed is that the number of crack propagations for a given test is relatively low (between 2 and 4 before compressive failure on the opposite side). This is uncommon for CT tests of this size; the number of crack propagations in the literature is usually around 10 [1,5].



5

Figure 13 : Crack length vs displacement for CT tests

The 3 methods to measure the crack length, detailed in previous sections, were applied to CT4 (the test was stopped to be able to estimate the crack length and detect secondary damage using X-ray tomography). The results are visible on Figure 14. The first conclusion here is that tomography and IR measurements seem to give consistent results. Moreover, it seems that by using IR images to estimate the crack length with the method detailed in 5.ii, and by defining the tip of the crack as failure in at least one 0° ply, the tip of the crack can be detected accurately (with a difference smaller than 0.2 mm). However, if the tip of the crack is defined as failure in all 0° plies, the difference is around 1.48 mm.

10

15

Results are not consistent for DIC measurement using a maximum strain criterion. A large propagation is detected before anything is visible on IR images. IR and DIC measurements are available for all specimens, and this behavior could be observed in multiple tests. This result can be explained by the failure scenario observed on CT specimens. Indeed, matrix cracking is observed before the first load drop and significant heating on the IR. This damage propagates along the surface 45° fibers, thus leading to a seemingly large strain in the y direction, ϵ_{yy} , caused by the discontinuity created by matrix failure. This matrix crack can be seen for CT4 for a crack length equal to 6.6 mm (IR measurement) on Figure 21 (a). The first conclusion that can be drawn is that DIC using a strain criterion does not seem to be a reliable measurement of the crack length with 45° plies on the surface for compact tension tests.

20

25

CT4 comparison between crack length measurement methods

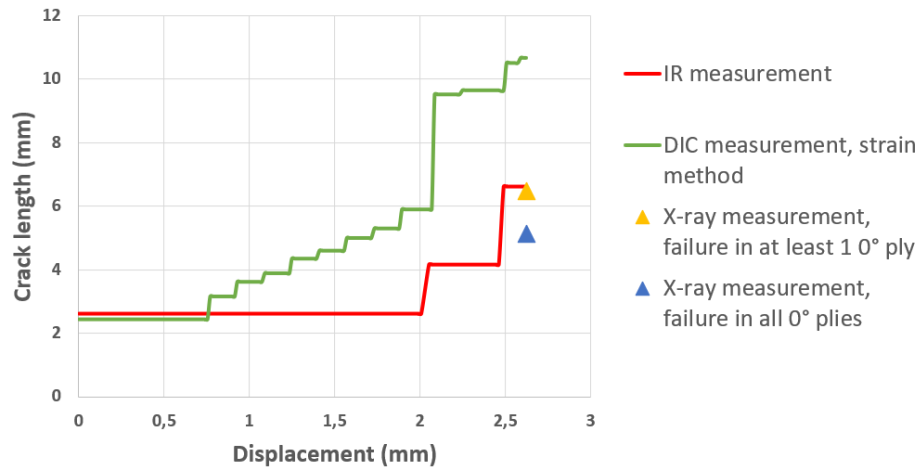
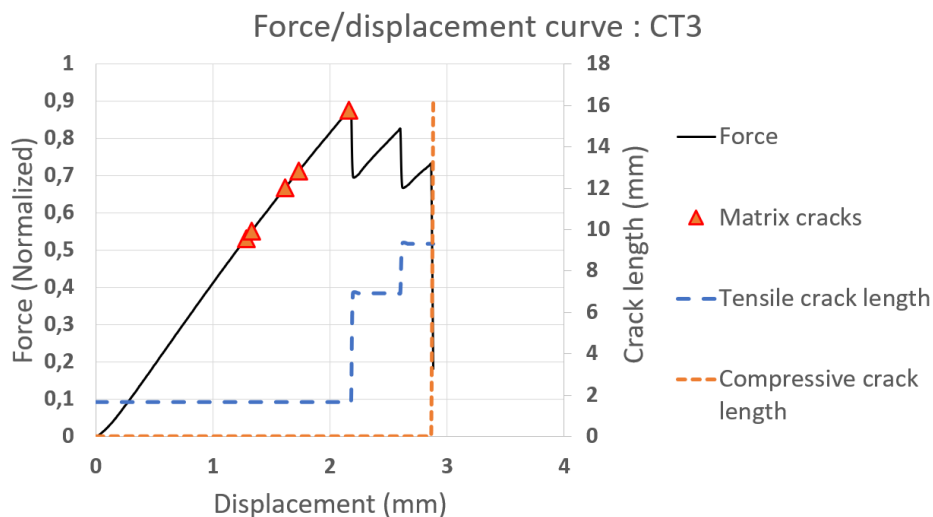


Figure 14 : Comparison of the different crack length measurement methods for CT4

4.3. Failure scenario

5 The understanding of the failure scenario is at stake for the next steps, as it allows the results to be understood and the calculations to be carried out correctly.

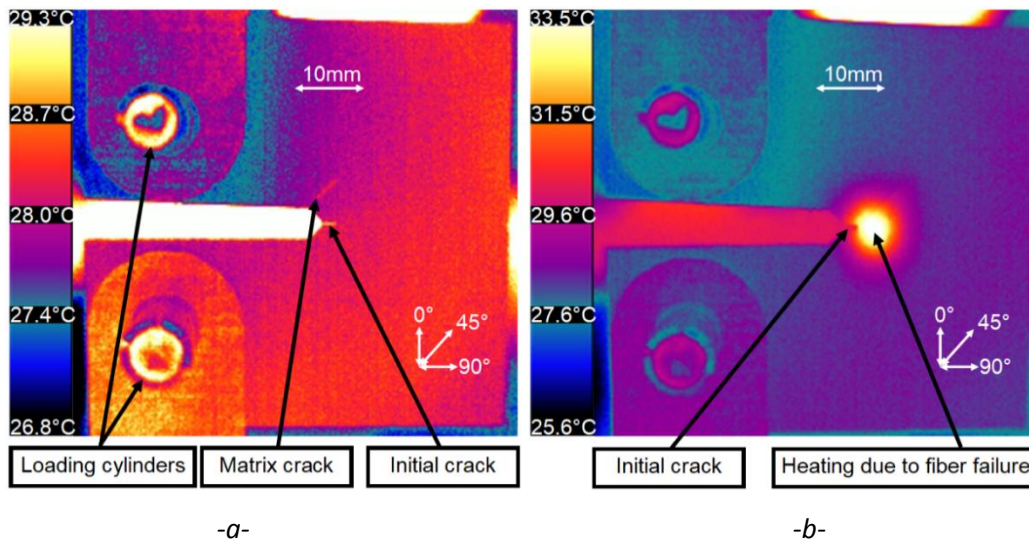
The failure scenario was observed to be the same for all CT tests, each failure following the same steps. The example of behavior that will be taken here is CT3 and thus can be generalized to all CT tests of both campaigns. The force displacement/curve and important steps can be seen in Figure 10 15. The tensile crack length corresponds to the propagation of the crack in tension, which is the phenomenon studied during CT tests. The compressive crack length can also be seen, corresponding to the final failure in compression on the other side of the specimen; for this reason its length is equal to 0 until the end of the test.



15 Figure 15 : Force/displacement curve of CT3, with the tensile and compressive crack lengths

Matrix cracks are the first observable damage (marked on the force/displacement curve with triangle-shaped marks), starting at a 1.3 mm displacement. The IR image is visible on Figure 16 (a). The heating follows the fiber orientation, and damage is located around the pre-crack. The amplitude of the heating is lower than 0.5°C, thus fiber failure can be excluded. These matrix cracks before the first fiber failure lead to a loss of stiffness of around 3%.

The second step is fiber failure, which leads to a clearly visible load drop and heating of around 4°C (Figure 16 (b)). On X-ray images of the stopped test CT4, a large delaminated area can be observed, particularly between the two +/-45° surface plies, as visible in Figure 17. The final step is the brutal compressive failure happening on the opposite side of the specimen, with a significant increase in the temperature in the area (Figure 18 (a)). Indeed, as can be seen in Figure 18 (b), a part of the specimen is loaded in tension and another part in compression.



15 Figure 16 : (a) IR image of matrix cracking on CT3 before the first crack propagation (surface ply at 45°), (b) IR image showing local heating due to the first crack propagation of CT3

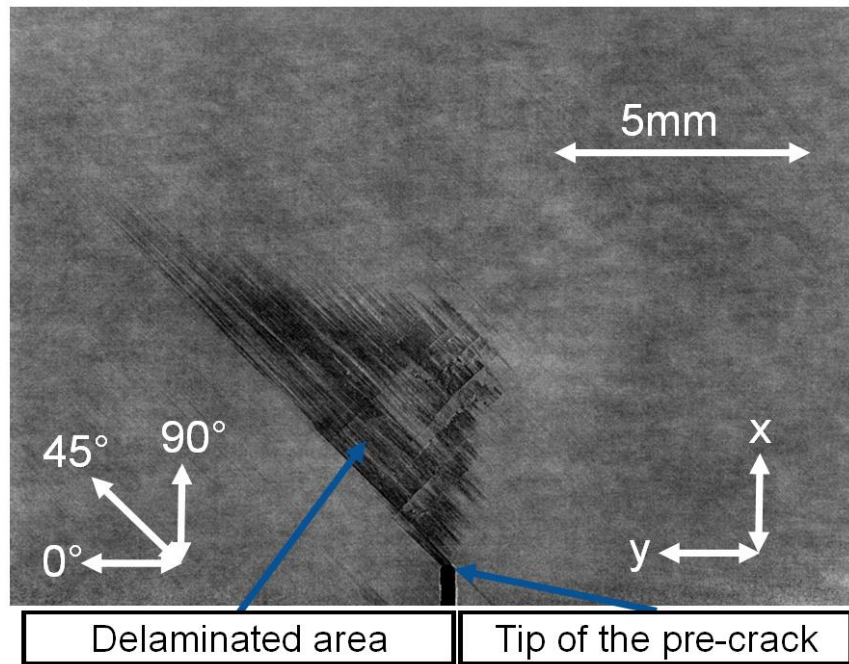


Figure 17 : X-ray tomography image showing delamination between 45 and -45° plies on CT4

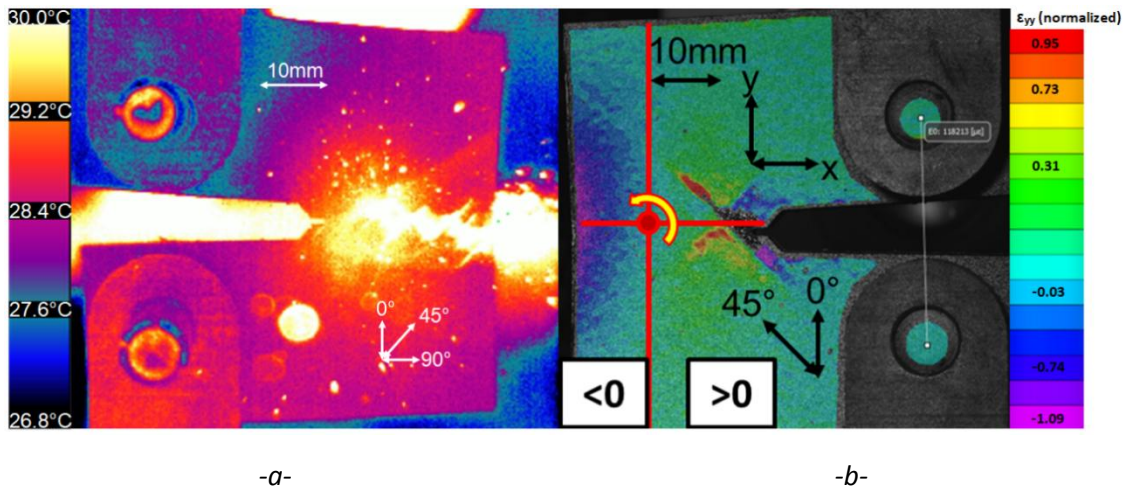


Figure 18 : (a) IR image of final compressive failure on CT3, (b) ϵ_{yy} strain field just before final compressive failure on CT3 showing tensile and compressive areas

5

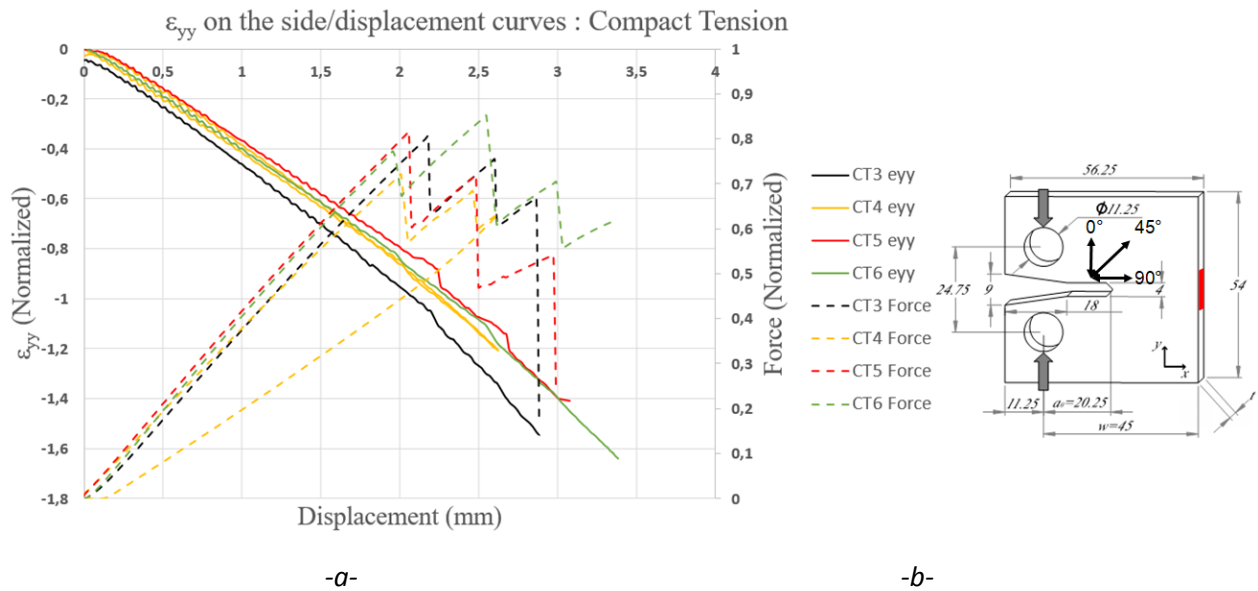
-a-

-b-

10 Secondary damage on CT specimens was monitored using IR images and by using the camera placed on the side of the specimen, strains on the side could be computed using Digital Image Correlation. The results are visible in Figure 19 (a), strains are averaged in a rectangle placed on the middle of the side of the specimen (Figure 19 (b)). For comparison, force/displacement curves are also plotted on a different scale. For confidentiality reasons, strains were normalized using the minimum strain acceptable by the fibers given by the manufacturer. The curve ends at the end of the test, i.e., when
 15 compressive failure happens for CT3, 5 and 6.

The first noticeable thing is that the strains measured just before compressive failure on CT3, 5 and 6 largely exceed the compressive strength of the material, between 40% and 60%. No noticeable heating of the specimen was detected on the side of the specimen. CT4 was stopped at a strain exceeding the compressive strength by 20%, and no damage was detected on X-ray tomography images. An explanation for this phenomenon could be the in-plane curvature, i.e. the ϵ_{yy} gradient along the x direction, visible on Figure 18 (b). It has been shown that out-of-plane curvature could impact the kink-band phenomenon and raise the value of the compressive failure strain of the material [23], and it is possible that in-plane curvature could also have an effect. However, the evolution of the compressive strength under in-plane curvature is still largely unknown, and specific tests are needed to fully understand this behavior.

No buckling of the specimen was detected using stereo-correlation, confirming the relevance of the use of 45° plies on the external part of the specimen.



15 Figure 19 : Strains on the side of the specimen vs displacement, compared to force/displacement curves (a), schematic showing the rectangle (in red) over which strains were averaged (b)

4.4. Computation of the critical strain energy release rate G_{IC_ply} for CT tests

Using ASTM and compliance methods, the SERR of the laminate G_{IC_lam} could be computed. Among the 3 interpolation formulas of C(a) tested, (Equation 3) gave the best results for all tests, with an average R^2 correlation coefficient equal to 0.99, against 0.93 for (Equation 1) and 0.96 for (Equation 2).

Once the value of G_{IC_lam} was estimated for the laminate, this value had to be computed for the ply using the rule of mixtures. The results are visible in Figure 20. The average value at initiation was obtained by calculating the average G_{IC_ply} of the ply of all tests and all methods, for the first value obtained on each test. ASTM and compliance methods seem to give consistent results, values seem to reach a plateau for a crack length superior to 7 mm. Moreover, all curves seem to follow the

same trend (except for CT2). However, a large dispersion on G_{IC_ply} at initiation can be noticed, particularly for the compliance method, with a variation coefficient equal to 37%. Both methods considered, the variation coefficient is equal to 26%. In the same way, the value of G_{IC_ply} during propagation shows a large dispersion, if a value of $a=7\text{ mm}$ is considered, then the variation coefficient is found to be equal to 17%.

Due to confidentiality issues, results were normalized using the maximum computed value for G_{IC_ply} in tension.

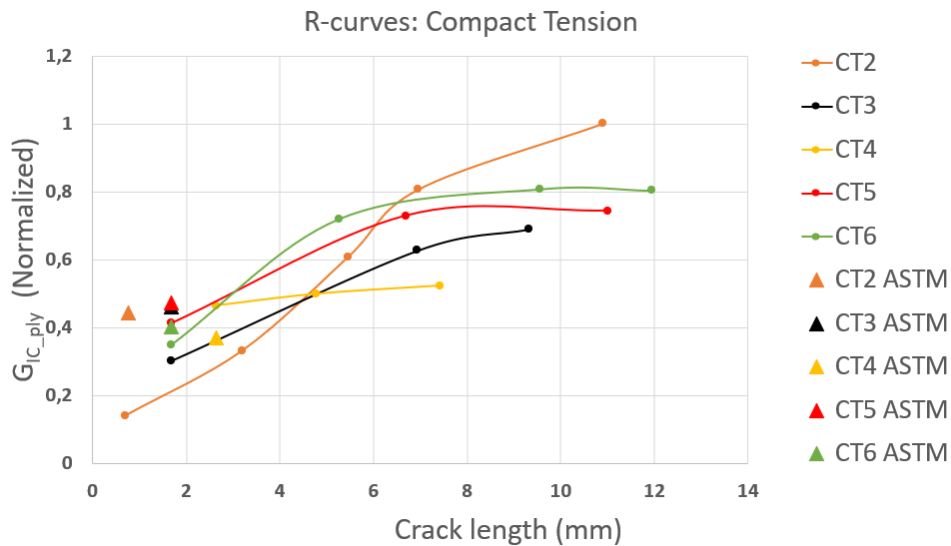


Figure 20 : strain energy release rate of the fibers vs crack length for CT tests using compliance and ASTM methods

10

The rule of mixtures assumes a step-like propagation in the $\pm 45^\circ$ plies (Figure 8). To check this assumption, X-ray images were extracted for the surface 45° ply (Figure 21 (a)), and for the -45° sub-surface ply (Figure 21 (b)). It can be concluded that the shape of propagation going successively through the matrix, parallel to the fibers, then perpendicularly to the fibers is justified for the sub-surface plies (Figure 21 (b)). However, the surface ply (Figure 21 (a)) shows no fiber failure, only matrix cracking propagating between the fibers can be observed. This can result in an under-estimation of G_{IC_ply} since the actual length of broken fibers is lower than the forecasted one.

15

Thus, a second rule of mixtures derived from (Equation 4) can be computed, where this time only two 45° plies are considered:

20

$$G_{IC_lam} = (8 G_{IC_ply} + \frac{2}{\sqrt{2}} G_{IC_ply}) / 20 \quad \Rightarrow \quad G_{IC_ply} = 2.12 * G_{IC_lam}$$

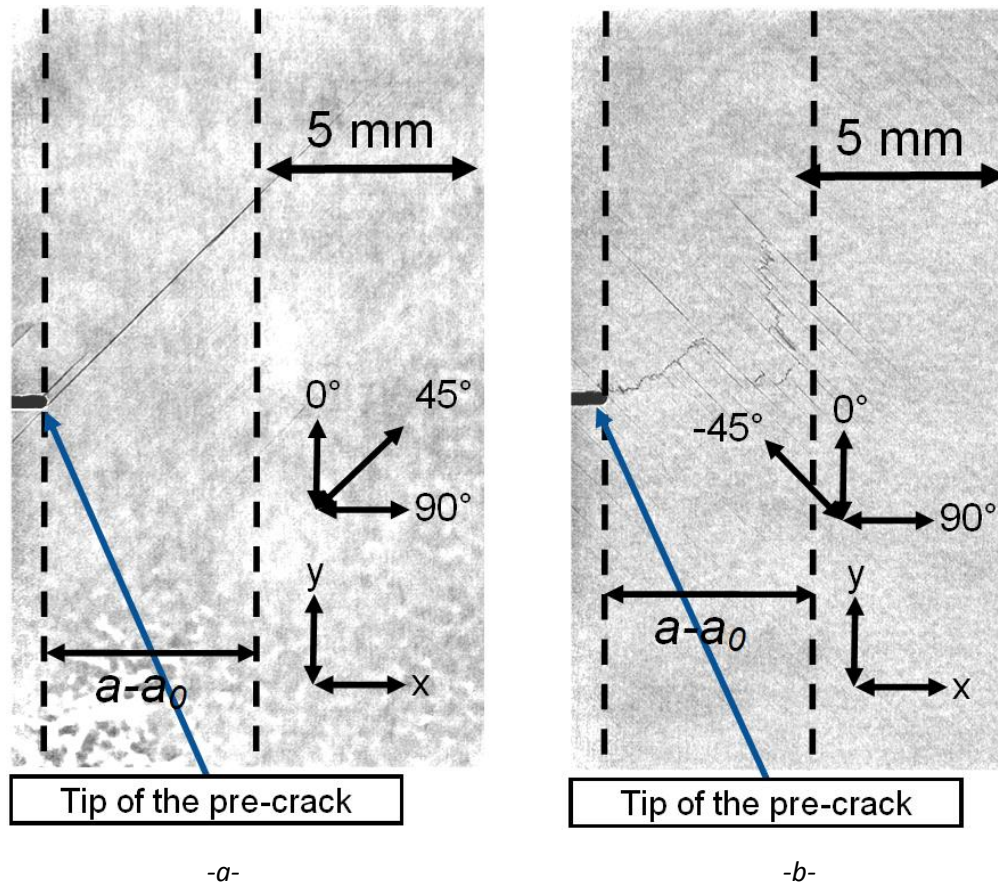


Figure 21 : X-ray tomography of CT4 of the crack propagation in a surface ply at 45° (a) and a sub-surface ply at -45° (b) The x-axis coordinate of the crack tip is indicated by the dotted line

5

Moreover, extensive delaminated areas were observed at 45°/-45° interfaces and -45°/0° interfaces (Figure 17). This can result in an over-estimation of G_{IC_ply} , since energy is dissipated through this mechanism and cannot be attributed to fiber failure. The relevance of the rule of mixtures can be discussed for this stacking sequence. The order of magnitude of the energy dissipated through this mechanism can be estimated on CT4, where X-ray microtomography images are available. The delaminated surface is measured, and delamination is assumed to propagate only in mode II (which is a conservative hypothesis). The obtained surface is thus multiplied by the SERR in mode II G_{IIc} , resulting in an estimation of the energy dissipated through delamination for this test and at this step of the crack propagation. Compared to the total dissipated energy, this results in a proportion of around 9% of the total dissipated energy from the beginning of the test. Finally, the error on the force due to the loss of stiffness caused by matrix cracking before the first crack propagation was estimated at 3%, which results in an error on F^2 and thus on G_{IC_ply} of around 6%.

By considering these three last phenomena, the value of G_{IC_ply} at initiation is re-estimated.

20 5. Compact Compression (CC) tests results

5.1. Force/displacement curves

Force/displacement curves for CC tests can be seen in Figure 22. CC1, 2 and 3 were loaded until the loading devices touch each other. CC4 and 6 were stopped just after the maximum force was reached and started to decrease, to study what happens just after the load drop. CC5 was stopped in the middle of the crack propagation to study the shape of the crack during propagation using X-ray tomography.

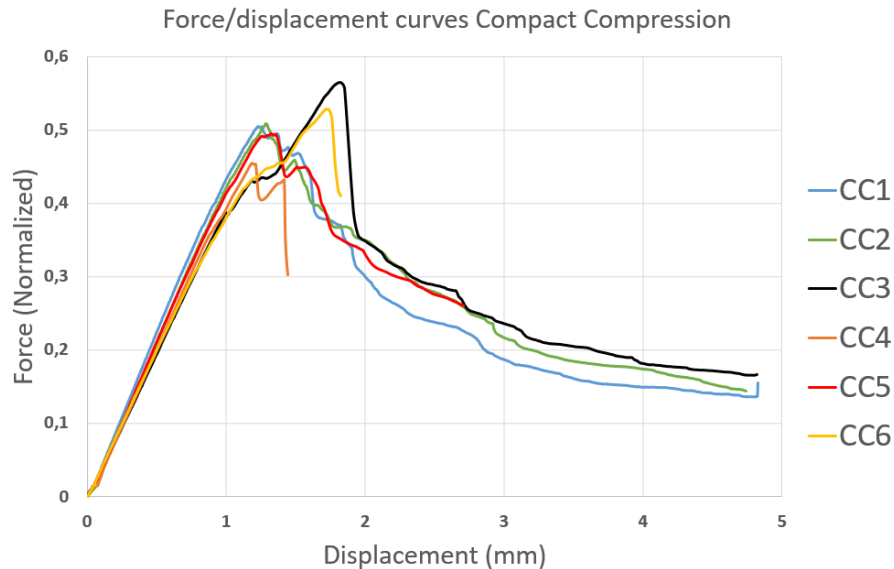


Figure 22 : Force/displacement curves for Compact Compression tests (normalized)

10 5.2. Crack length/displacement curves

Crack length vs displacement curves could be first estimated using IR images, results can be seen on Figure 23. CC tests show a low dispersion of the displacement associated with the first crack propagation, with a RSD equal to 7.8% around a mean value of 0.59 mm. An IR image illustrating the first crack propagation can be seen in Figure 25 (a). The first noticeable thing is that the crack propagates before anything is clearly visible on the force/displacement curve (Figure 22, for a displacement equal to 0.6 mm).

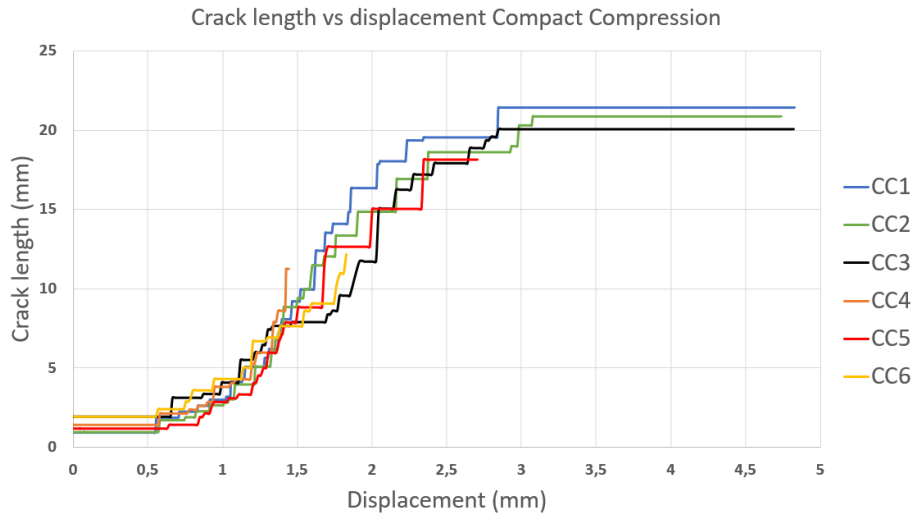
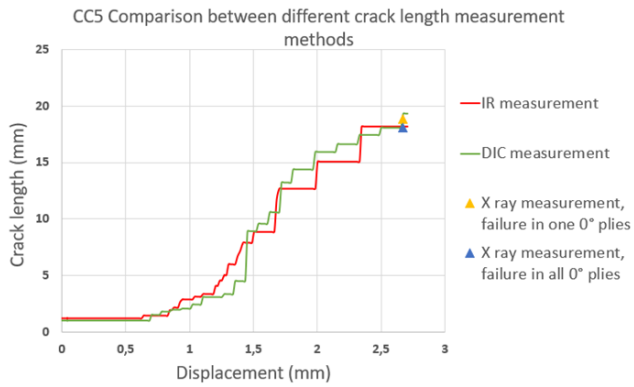
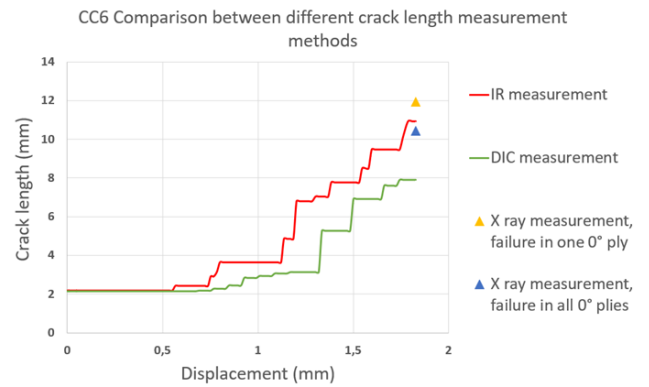


Figure 23 : Crack length/displacement curves for Compact Compression tests, using IR measurement



-a-



-b-

Figure 24 : Comparison of the different crack length measurement methods for CC5 (a) and CC6 (b)

The comparison between IR, DIC and X-ray tomography can be carried out on CC5 and 6; the result is visible in Figure 24. The difference between the two possible definitions of the crack length using X-ray tomography (at least one damaged 0° ply or all plies are damaged) is around 1 mm (which is the same order of magnitude as that observed on CT). Contrary to CT tests, the crack length measured with IR images seems to be the average of these two lengths.

Measurements made with DIC using a minimum strain criterion gave consistent results for CC1-5. However, IR and DIC measurements were not in line for CC6, but since X-ray tomography and IR measurements result in the same final crack length, a greater trust can be placed in the IR measurement than in the DIC. The displacement at initiation was roughly the same using both techniques, with an average difference equal to 0.14 mm. Thus, IR imaging seems to be an easy and reliable way of estimating the crack length.

5.3. Failure scenario

Two main force/displacement shapes can be identified. CC1, 2 and 5 exhibit a maximum in the curve followed by a smooth decrease in the force. On the contrary, CC3, 5 and 6 show a force peak followed by a brutal decrease in the force, and significant heating on IR images. Moreover, the maximum force is noticeably higher (around 8%) and reached for a higher displacement (around 28%) for CC3 and 6 compared to other tests. CC4 seems to combine both failure scenarios: it shows a low force peak occurring at a displacement close to CC3, 5 and 6, but exhibits two successive load peaks, the second one being followed by a load drop comparable to that observed after the load peak for CC3 and 6. In any case, the load drop is accompanied by a significant heating of the specimen, as can be seen in Figure 25 (b). For each failure scenario, tests showed a low dispersion. CC1, 2 and 5 maximum average normalized force was equal to 0.467 with an RSD of 1.6%. The difference between CC3 and 6 force peaks was 6.3%. However, the difference between these two failure scenarios was 8% for the force and 28% for the displacement. Despite the different failure scenarios, forces measured for a 2 mm displacement are close. Indeed, CC1, 2, 3 and 5 seem to follow the same trend, and show an RSD equal to approximately 10% between 2 and 4.5 mm displacements. Phenomena leading to these different failure scenarios are not fully understood yet; however, they seem to be correlated to the pre-crack length (CC3 and 6 pre-crack lengths were around 40% longer than other pre-cracks due to manufacturing inaccuracies). Moreover, the load increase just before the force peaks does not seem to be linked to the pre-crack closure.

Despite the numerous different behaviors noticed previously on force/displacement curves, crack length/displacement curves show no great difference between different failure scenarios. However, for the interval of displacement where differences on the force curves could be observed (between 1.2 and 2 mm), CC3 and 6 crack lengths seem to be lower than other tests, especially between 1.5 and 2 mm. All tests seem to converge to the same crack length between 20 and 21.5 mm for high displacement values, which is in line with the fact that force curves converge to the same values with the same trend.

The shape of the crack for different distances between the tip of the pre-crack and the cut view obtained using X-ray tomography can give information about the processes taking place during crack propagation. The shape of the tip of the crack (i.e. for a distance between the tip of the crack to the image equal to 18.8 mm) can be seen in Figure 26. Two main failure phenomena are visible, the first matrix cracking in 90° plies at around 45°, which is typical of matrix failure under transverse compressive loading. These matrix cracks result in delamination between +/-45° plies. Secondly, blurry areas can be seen between matrix cracks, and can be attributed to kink bands, or more probably fiber failure (the size of the voxel being too large to make the difference with certainty). The shape of the beginning of the crack is visible in Figure 27, with a distance from the pre-crack tip equal to 1.74 mm (with a total crack length equal to 18.8 mm). This image shows the same profile as that described by Zobeiry et al. [24], with slip surfaces and splittings in 0° plies, and crushed material gathered in numerous regions which eventually open the material through delamination (“wedge effect”). These large, delaminated areas could also be observed on CC6 (stopped just after the load drop) and are believed to be the reason for the load drop observed in these tests. Thus, the value of the critical SERR can only be measured at initiation. Indeed, when the crack starts propagating, phenomena other than fiber failure in compression take place and artificially raise the measured value of $G_{IC,ply}$. Pinho et al. [4] and Catalanotti et al. [6] came to the same conclusion that CC tests are unsuitable for computing compression R-curves.

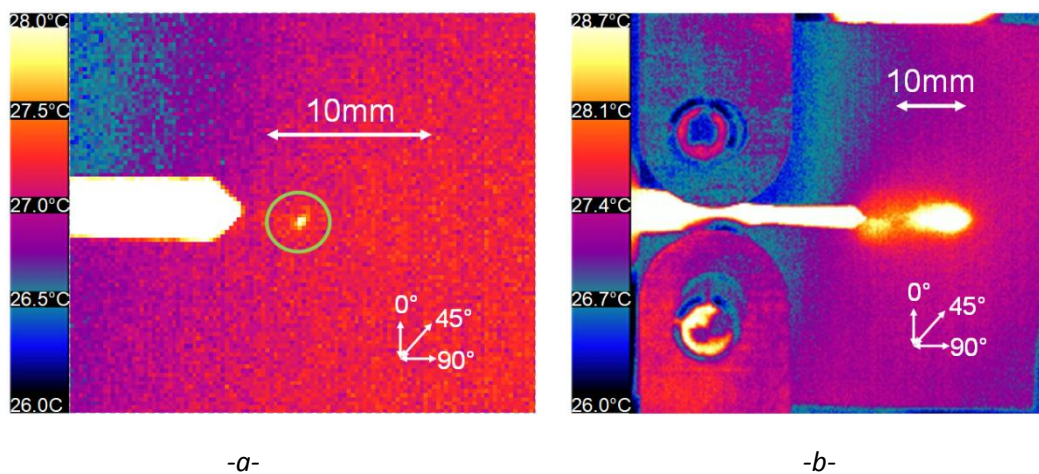


Figure 25 : Heating due to crack propagation on CC6, for the first crack propagation (a) or the load drop (b)

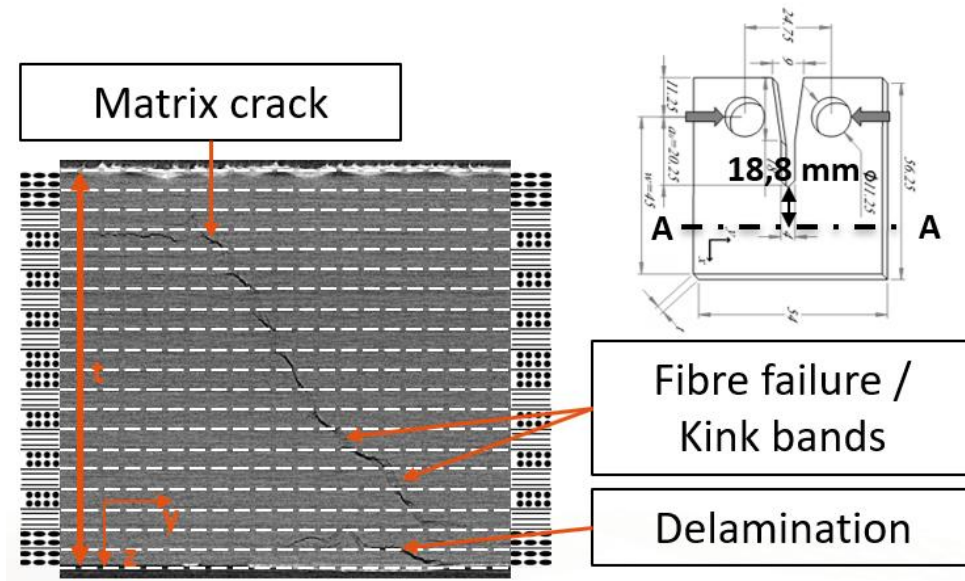


Figure 26 : A-A cut of the shape of the tip of the crack on CC5, several 0° plies exhibiting fiber failure

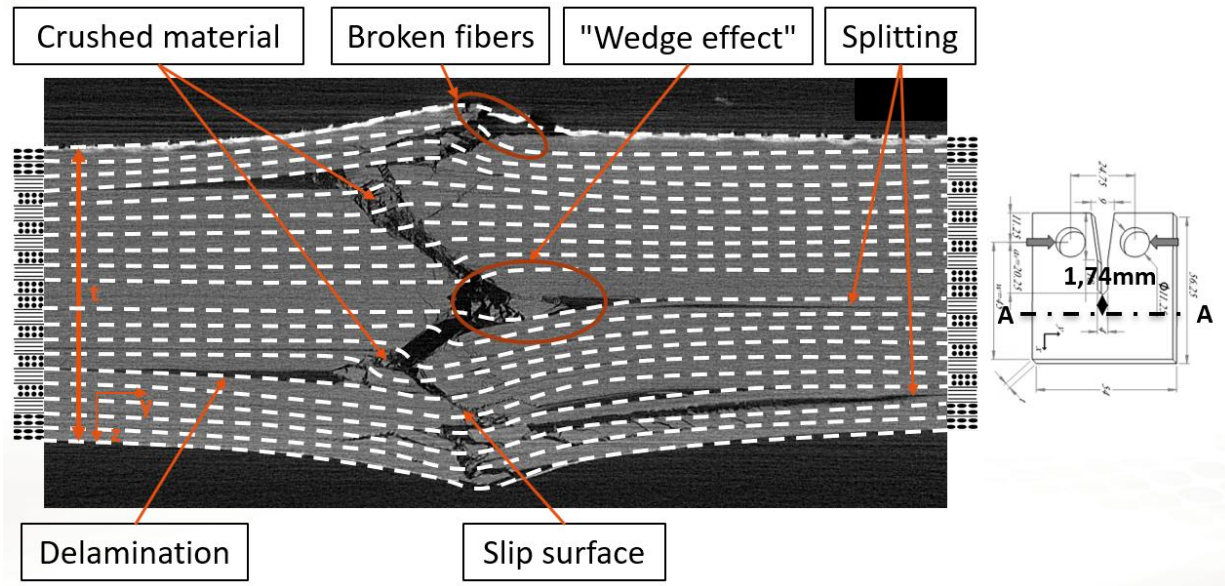


Figure 27 : A-A cut of CC5 showing damage after the crack has passed onto a region

5

Secondary damage (bearing around the loading holes, tensile damage on the opposite side of the specimen) could not be detected in IR images (no detectable heating in the tensile area of the specimen), nor visually after the test. Moreover, strains measured on the side of the specimen did not exceed the maximum strain acceptable by the fibers. However, matrix cracking could be observed in X-ray tomography for CC5 in 90° plies (Figure 28). Such damage could not be detected for CC6; thus, it can be assumed that they happen late during the crack propagation phase, and we can conclude that they should not have any noticeable effect on the computation of G_{IC_ply} .

10

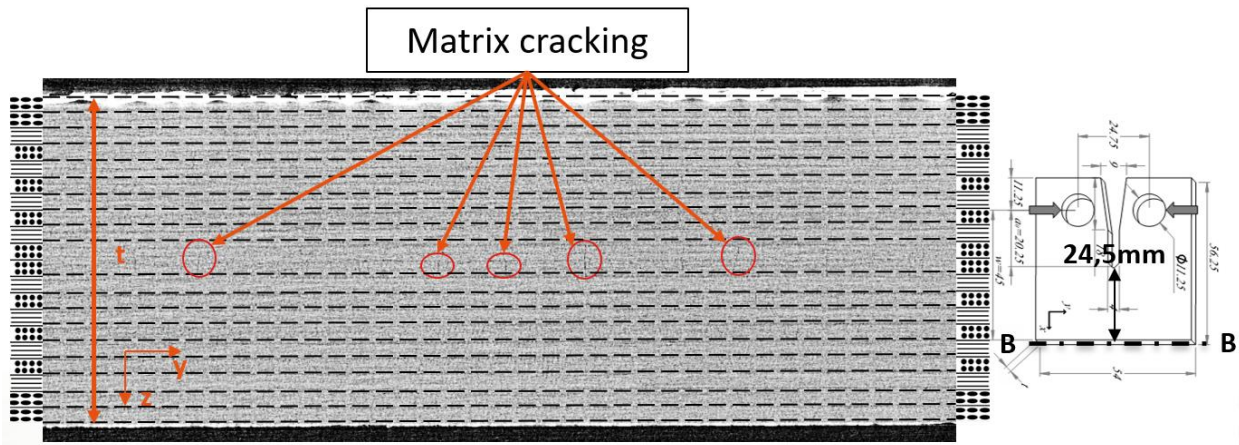


Figure 28 : B-B cut of CC 5 showing secondary damage (matrix cracking) on the opposite side of the specimen

5.4. Computation of the critical strain energy release rate G_{IC_ply}

- 5 As for CT tests, R-curves for CC tests could be computed and are visible on Figure 29. Due to confidentiality issues, results were normalized using the maximum computed value for G_{IC_ply} in tension. Among the 3 interpolation formulas of $C(a)$ tested, (Equation 3) gave the best results for all tests, with an average R^2 correlation coefficient equal to 0.98, compared to 0.89 for (Equation 1) and 0.91 for (Equation 2).
- 10 As for CT tests, the interesting value is the critical SERR of the ply G_{IC_ply} , and it can be computed using the rule of mixtures. The ASTM method seems to give consistent and repeatable results, with a variation coefficient equal to 12%. This can be explained by the very low dispersion of forces and displacements associated with the first crack propagations on CC tests, as shown in Figure 29. The compliance method seems to give more dispersed results, with a RSD equal to 83%. This large
- 15 dispersion can be explained by the fact that two curves (CC2 & 6) have very low initiation values.

As detailed in 5.3, the value in propagation is artificially raised by other phenomena (crushing, plasticity etc.) taking place in areas where the crack has already propagated, thus the G_{IC_ply} measured is the sum of the energy needed to propagate the crack and to crush material. The first conclusion from these curves is that during propagation the energy dissipated by crack propagation

20 seems to be only a small part of the total dissipated energy, since there is a factor of around 10 between G_{IC_ply} at initiation and propagation. R-curves are different for the different failure scenarios highlighted in 5.1 for crack lengths between 7 and 12 mm (corresponding to displacements between 1.2 and 2 mm). Indeed, CC3 and 6 showed a load increase for these displacements, and R-curves also show an increase of G_{IC_ply} when the load increases.

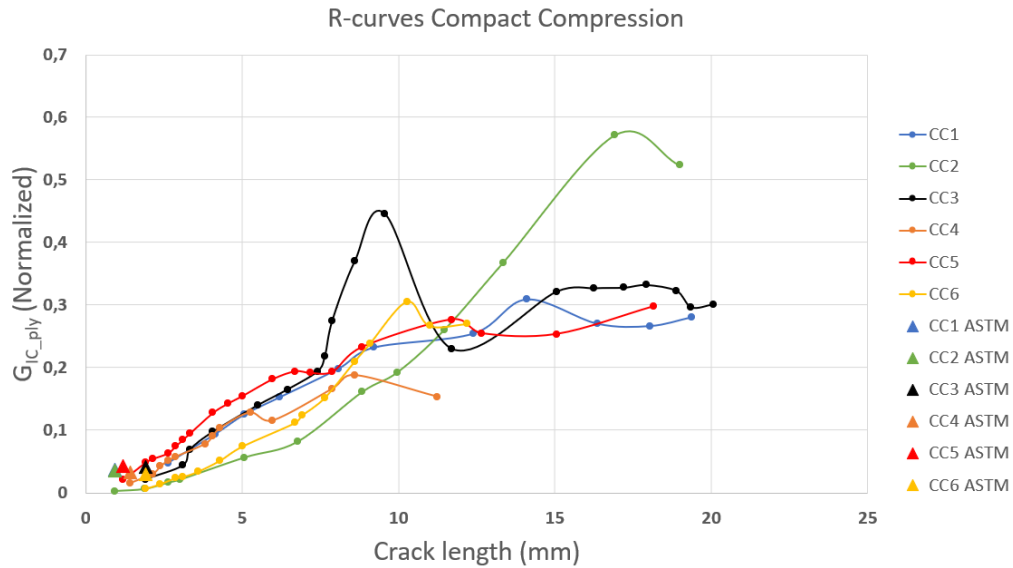


Figure 29 : R-curve of the laminate for CC tests

The propagation in $\pm 45^\circ$ plies can be seen in Figure 30. The step-like propagation described in Figure 8 and used to compute the length of broken fibers can be observed in both 45° plies. There seems to be more matrix cracking than that forecast by the step-like model (extensive matrix cracking around the edges of the “steps”), especially once the crack has propagated around 5 mm. Due to the low value of G_{IC_ply} , these matrix cracks may be non-negligible and can participate in the G_{IC_ply} increase with the crack length.

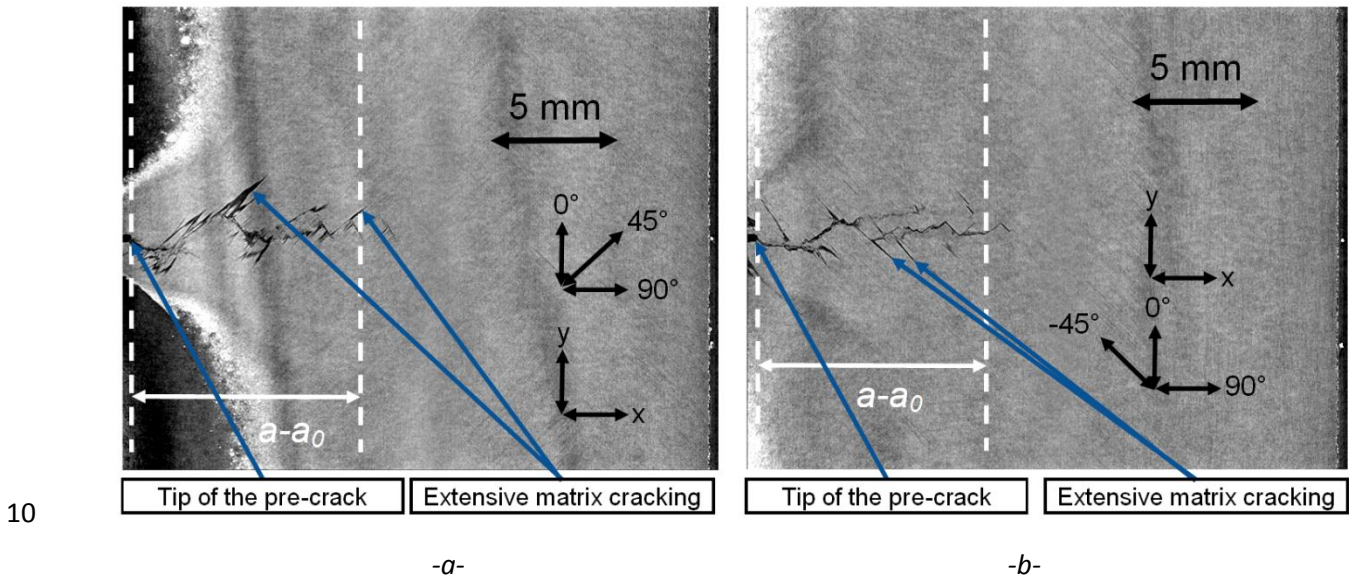


Figure 30 : X-ray tomography of CC6 of the crack propagation in a surface ply at 45° (a) and a sub-surface ply at -45° (b)

15 6. Comparison of the values with the literature

6.1. Compact Tension tests

Values for the strain energy release rate of the ply for thermoset carbon fibers composites can be found in the literature and are summed up on Table 2.

CT tests: literature review	G_{IC_ply}(initiation)	G_{IC_ply} (propagation)
Pinho et al. [4]	91.6 kJ/m ²	133 kJ/m ²
Laffan et al. [5]	41-90 kJ/m ²	57-132 kJ/m ²
Catalanotti et al. [6]	98.7 kJ/m ²	133.7 kJ/m ²
Teixeira et al. [1]	46-104 kJ/m ²	49-160 kJ/m ²

Table 2 : Critical SERR values for carbon fibers/epoxy materials

5

The average value obtained at initiation for the G_{IC_ply} was found to be significantly higher than in the literature (even if the exact value cannot be given for confidentiality reasons). Similarly, the average value in propagation is substantially higher. The reason for this difference is not fully understood; however, the complexity of the failure scenario may influence this value. Moreover the fracture toughness is known to be dependent on the draping sequence, and the choice of the $\pm 45^\circ$ outside ply made for this study should affect the results. Indeed, this choice was made in order to limit the shear plasticity and increase the buckling load, but the values in the literature are classically performed with cross ply laminates (only 0 and 90° ply). It would be interesting to repeat these experiments with cross ply laminates in order to compare the values obtained. Furthermore, a new material with a possibly better carbon fiber/matrix cohesion may substantially raise the value of the critical SERR.

Moreover, for certain tests, damage around the crack propagation could be detected near the end of the test (for crack lengths superior to 7mm), as visible in Figure 31. Indeed, the white arrow indicates the crack length one second before the heating happened, thus showing that damage detected by this heating does not correspond to crack propagation as damage is not happening further from the initial crack.

20

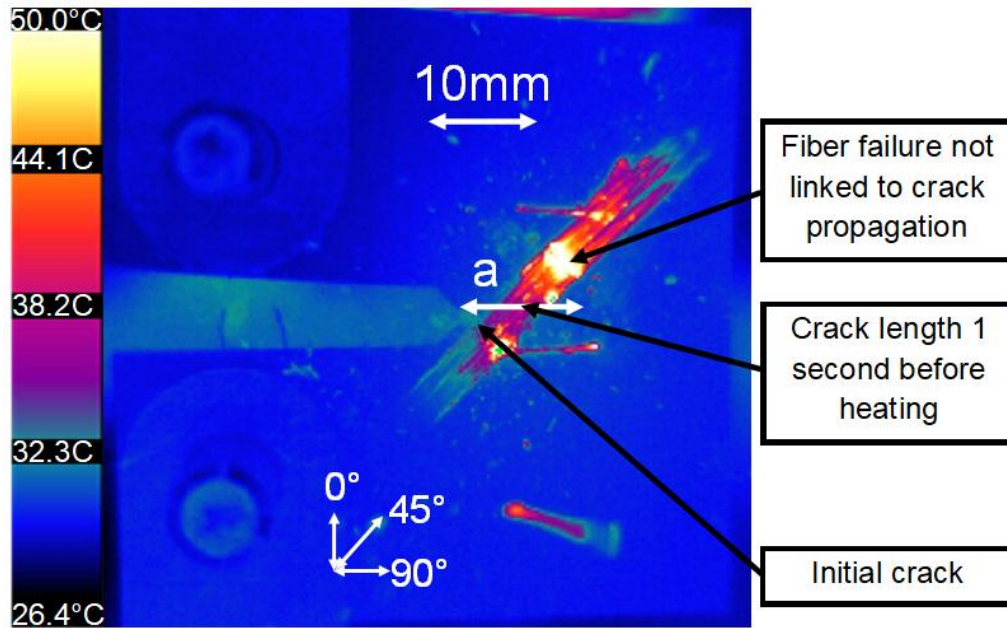


Figure 31 : IR image of CT5 showing numerous damages around the crack

5 All phenomena detailed in this part and their consequences for G_{IC_ply} computation for CT tests are detailed in Table 3.

Phenomenon	Effect on the G_{IC_ply} in tension if not accounted in computation
Matrix cracking before the first crack propagation (loss of stiffness)	Decreases G_{IC_ply} at initiation by about 6%. During propagation, it can be assumed that the effect remains during propagation.
Damage around the crack growth during propagation (Figure 31)	Increases G_{IC_ply} at the end of the propagation, difficult to estimate quantitatively
Extensive delamination (Figure 17)	Increases G_{IC_ply} in propagation by about 9%
No fiber failure in 45° outside ply (Figure 21)	Decreases G_{IC_ply} at initiation and in propagation by about 13%

Table 3 : phenomena which can influence the computation of the critical SERR for CT tests

6.2. Compact Compression tests

10 As demonstrated in previous sections, only the value at initiation is valid. Fewer values of the critical SERR at initiation for CC are available in the literature. Pinho et al. [4] obtained a value equal to 79.9 kJ/m², Catalanotti et al. [6] obtained 47.5 kJ/m². On average, the value of G_{IC_ply} was found to be significantly lower than literature values. A possible explanation is that the use of IR measurements

means that damage is detected sooner than with other techniques, thus the computed value of G_{IC_ply} is lower. Indeed, if the load drop is considered as the critical force and the moment when the crack starts propagating and crack propagation is visually measurable on the surface, the value obtained is this time in line with other studies. Moreover, as previously evoked, the choice of the $\pm 45^\circ$ outside ply made for this study should affect the results compared to the classical cross ply laminates (only 0 and 90° ply) in the literature.

It is interesting to mention that with other experimental setups, the value obtained is closer to the values described in this paper. Using notched compression setup and a layup composed of only 0° plies, Sutcliffe and Fleck [25] found a value for G_{IC_ply} between 10 and 17 kJ/m^2 . In the same way, Laffan et al. [12] found a value of around 25.9 kJ/m^2 using a four point bending testing configuration.

All phenomena detailed in this part and their effects on G_{IC_ply} computation for CC tests are detailed in Table 4.

Phenomenon	Effect on the G_{IC_ply} in compression computation
Crushing	Raises G_{IC_ply} in propagation
Late detection of crack propagation	Raises G_{IC_ply} at initiation

Table 4 : phenomena which can influence the computation of the critical SERR for CC tests

15

7. Conclusion

Translaminar failure (at the scale of the laminate) has been studied extensively the main goal being to compute the critical strain energy release rate in mode I of the ply G_{IC_ply} using CT and CC specimens. The G_{IC_ply} value for CT tests could be obtained using the rule of mixtures, modified using actual damage observed using X-ray tomography images. This value was found to be higher than in the literature. The value in propagation was found to be much higher than in other studies. The value for CC tests is only reliable at initiation, but with a large dispersion on the value. This value is lower than in other CC studies but is in line with values obtained using other test setups.

25

The presence of 45° plies on the outside of the stacking sequence proved to be beneficial for CT and CC tests, while being more representative of real-life stacking sequences used in the industry. Indeed, no buckling of the specimen was detected, confirming the interest of placing these plies on the outside of the stacking sequences. Moreover, no large plasticity of the matrix before the first fiber failure was observed. Nevertheless, these $\pm 45^\circ$ outside plies should affect the evaluation of the fracture toughness and make it difficult to compare with the values in the literature where the tests are performed with more classical draping sequences composed of cross ply (only 0 and 90° ply). It

30

would be interesting to repeat these experiments with cross ply laminates in order to compare the values obtained.

IR images to estimate the crack length proved to be a reliable and easy way to measure the crack length, as it can see damage inside the laminate and is able to show damage history, thus allowing stacking sequences with no 0° or 90° plies on the outside. X-ray microtomography and IR crack length measurements gave consistent results, boosting trust in the use of IR images from a qualitative point of view.

The last step is to model the failure of these tests using the finite elements method, as it would allow the separation of all sources of energy dissipation, and finally measure the G_{IC_ply} using inverse methods.

8. References

- [1] Teixeira, R. D. F., Pinho, S. T., & Robinson, P. (2014). Translaminar fracture toughness of CFRP: from the toughness of individual plies to the toughness of the laminate (Doctoral dissertation, Imperial College London)
- [2] Pujols Gonzalez, J.D., Vieille, B., Bouvet, C., 2021. High temperature translaminar fracture of woven-ply thermoplastic laminates in tension and in compression. Engineering Fracture Mechanics 246, 107616. <https://doi.org/10.1016/j.engfracmech.2021.107616>
- [3] Blanco, N., Trias, D., Pinho, S.T., Robinson, P., 2014. Intralaminar fracture toughness characterisation of woven composite laminates. Part I: Design and analysis of a compact tension (CT) specimen. Engineering Fracture Mechanics 131, 349–360. <https://doi.org/10.1016/j.engfracmech.2014.08.012>
- [4] Pinho, S.T., Robinson, P., Iannucci, L., 2006. Fracture toughness of the tensile and compressive fibre failure modes in laminated composites. Composites Science and Technology 66, 2069–2079. <https://doi.org/10.1016/j.compscitech.2005.12.023>
- [5] Laffan, M.J., Pinho, S.T., Robinson, P., Iannucci, L., 2010. Measurement of the in situ ply fracture toughness associated with mode I fibre tensile failure in FRP. Part II: Size and lay-up effects. Composites Science and Technology 70, 614–621. <https://doi.org/10.1016/j.compscitech.2009.12.011>
- [6] Catalanotti, G., Camanho, P.P., Xavier, J., Dávila, C.G., Marques, A.T., 2010. Measurement of resistance curves in the longitudinal failure of composites using digital image correlation. Composites Science and Technology 70, 1986–1993. <https://doi.org/10.1016/j.compscitech.2010.07.022>
- [7] Reiner, J., Chen, C., Vaziri, R., Poursartip, A., 2022. Combining digital image correlation and phased-array ultrasonics for non-destructive testing of translaminar fracture in composite laminates. Composites Part A: Applied Science and Manufacturing 161, 107060. <https://doi.org/10.1016/j.compositesa.2022.107060>
- [8] Gonzáles, L., Knauss, W.G., 2002. Scaling global fracture behavior of structures-sized laminated composites. International Journal of Fracture 118, 363-394. <https://doi.org/10.1023/A:1023351115322>
- [9] Saadati, Y., Bouvet, C., Chatelain, J.-F., Beauchamp, Y., 2020. Study of translaminar fracture toughness of unidirectional flax/epoxy composite. Composites Part C: Open Access 1, 100008. <https://doi.org/10.1016/j.jcomc.2020.100008>
- [10] Lisle, T., Bouvet, C., Hongkarnjanakul, N., Pastor, M.-L., Rivallant, S., Margueres, P., 2015. Measure of fracture toughness of compressive fiber failure in composite structures using infrared thermography. Composites Science and Technology 112, 22–33. <https://doi.org/10.1016/j.compscitech.2015.03.005>

- [11] Gutkin, R., Green, C.J., Vangrattanachai, S., Pinho, S.T., Robinson, P., Curtis, P.T., 2011. On acoustic emission for failure investigation in CFRP: Pattern recognition and peak frequency analyses. *Mechanical Systems and Signal Processing* 25, 1393–1407. <https://doi.org/10.1016/j.ymssp.2010.11.014>
- [12] Laffan, M.J., Pinho, S.T., Robinson, P., Iannucci, L., McMillan, A.J., 2012. Measurement of the fracture toughness associated with the longitudinal fibre compressive failure mode of laminated composites. *Composites Part A: Applied Science and Manufacturing* 43, 1930–1938. <https://doi.org/10.1016/j.compositesa.2012.04.009>
- [13] Laffan, M.J., Pinho, S.T., Robinson, P., McMillan, A.J., 2012. Translaminar fracture toughness testing of composites: A review. *Polymer Testing* 31, 481–489. <https://doi.org/10.1016/j.polymertesting.2012.01.002>
- [14] Dávila, C.G., Rose, C.A., Camanho, P.P., 2009. A procedure for superposing linear cohesive laws to represent multiple damage mechanisms in the fracture of composites. *International Journal of Fracture* 158, 211–223. <https://doi.org/10.1007/s10704-009-9366-z>
- [15] Blanco, N., Pinho, S.T., Robinson, P., 2006. Parametric analysis of different compact tension specimens for fracture toughness characterisation in woven composite materials. Report for the scientific sojourn at the Imperial College London, Gran Bretanya, from July until November 2006. <https://www.recercat.cat/handle/2072/4267>
- [16] McKinley, T.A., Carpenter, K.T., Parmigiani, J.P., 2018. Development of Novel Compact Compression Specimen for Matrix Compression Damage Initiation and Propagation Behavior in Fiber Reinforced Composites, in: *Volume 9: Mechanics of Solids, Structures, and Fluids*. Presented at the ASME 2018 International Mechanical Engineering Congress and Exposition, American Society of Mechanical Engineers, Pittsburgh, Pennsylvania, USA, p. V009T12A048. <https://doi.org/10.1115/IMECE2018-87106>
- [17] Reu, P., 2014. All about Speckles: Aliasing. *Experimental Techniques* 38, 1–3. <https://doi.org/10.1111/ext.12111>
- [18] Ortega, A., Maimí, P., González, E.V., Sainz de Aja, J.R., de la Escalera, F.M., Cruz, P., 2017. Translaminar fracture toughness of interply hybrid laminates under tensile and compressive loads. *Composites Science and Technology* 143, 1–12. <https://doi.org/10.1016/j.compscitech.2017.02.029>
- [19] Ortega, A., Maimí, P., González, E.V., Ripoll LI. 2014. Compact tension specimen for orthotropic materials. *Composites Part A: Applied Science and Manufacturing* 63, 85–93. <https://doi.org/10.1016/j.compositesa.2014.04.012>
- [20] Standard, A. S. T. M. E399-12, 2012. Standard Test Method for Linear-elastic Plane-strain Fracture Toughness K_{IC} of Metallic Materials, American Society for Testing and Materials, West Conshohocken, PA.
- [21] Tada, H., Paris, P. C., & Irwin, G. R. (2000). *The stress analysis of cracks*. Handbook, Del Research Corporation
- [22] Hao Wen, Jing Ma, Meiju Zhang, Guimei Ma, 2012. The comparison research of nonlinear curve fitting in Matlab and LabVIEW, in: *2012 IEEE Symposium on Electrical & Electronics Engineering (EEESYM)*. Presented at the 2012 IEEE Symposium on Electrical & Electronics Engineering (EEESYM), IEEE, Kuala Lumpur, Malaysia, pp. 74–77. <https://doi.org/10.1109/EEESym.2012.6258591>
- [23] Wisnom, M.R., Atkinson, J.W., 1997. Constrained buckling tests show increasing compressive strain to failure with increasing strain gradient. *Composites Part A: Applied Science and Manufacturing* 28, 959–964. [https://doi.org/10.1016/S1359-835X\(97\)00067-5](https://doi.org/10.1016/S1359-835X(97)00067-5)
- [24] Zobeiry, N., Vaziri, R., Poursartip, A., 2015. Characterization of strain-softening behavior and failure mechanisms of composites under tension and compression. *Composites Part A: Applied Science and Manufacturing* 68, 29–41. <https://doi.org/10.1016/j.compositesa.2014.09.009>
- [25] Sutcliffe, M.P.F., Fleck, N.A., 1994. Microbuckle propagation in carbon fibre-epoxy composites. *Acta Metallurgica et Materialia* 42, 2219–2231. [https://doi.org/10.1016/0956-7151\(94\)90301-8](https://doi.org/10.1016/0956-7151(94)90301-8)

[26] El-Sagheer, I., Abd-Elhady, A.A., Sallam, H.E.L.M., Naga, S.A.R., 2021. An Assessment of ASTM E1922 for Measuring the Translaminar Fracture Toughness of Laminated Polymer Matrix Composite Materials. *Polymers* 13(18). <https://doi.org/10.3390/polym13183129>